Monthly Notices
of the
ROYAL ASTRONOMICAL SOCIETY

MNRAS **472,** 447–464 (2017)
Advance Access publication 2017 August 2

doi:10.1093/mnras/stx1666

Cloud formation in metal-rich atmospheres of hot super-Earths like 55 Cnc e and CoRoT7b

G. Mahapatra,[1] Ch. Helling[1]★ and Y. Miguel[2]

[1]*Centre for Exoplanet Science, SUPA, School of Physics and Astronomy, University of St. Andrews, St. Andrews KY16 9SS, UK*
[2]*Laboratoire Lagrange, UMR 7293, Universite de Nice-Sophia Antipolis, CNRS, Observatoire de la Côte d'Azur, Blvd de l'Observatoire, CS 34229, F-06304 Nice cedex 4, France*

Accepted 2017 August 2. Received 2017 June 23; in original form 2017 March 9

ABSTRACT

Clouds form in the atmospheres of planets where they can determine the observable spectra, the albedo and phase curves. Cloud properties are determined by the local thermodynamical and chemical conditions of an atmospheric gas. A retrieval of gas abundances requires a comprehension of the cloud formation mechanisms under varying chemical conditions. With the aim of studying cloud formation in metal-rich atmospheres, we explore the possibility of clouds in evaporating exoplanets like CoRoT-7b and 55 Cancri e (55 Cnc e) in comparison to a generic set of solar abundances and the metal-rich gas giant HD 149026b. We assess the impact of metal-rich, non-solar element abundances on the gas-phase chemistry, and apply our kinetic, non-equilibrium cloud formation model to study cloud structures and their details. We provide an overview of global cloud properties in terms of material compositions, maximum particle formation rates and average cloud particle sizes for various sets of rocky element abundances. Our results suggest that the conditions on 55 Cnc e and HD 149026b should allow the formation of mineral clouds in their atmosphere. The high temperatures on some hot rocky super-Earths (e.g. the day side of CoRoT-7b) result in an ionized atmospheric gas, and they prevent gas condensation, making cloud formation unlikely on its day side.

Key words: astrochemistry – solid state: refractory – solid state: volatile – methods: numerical – planets and satellites: atmospheres.

1 INTRODUCTION

With telescopes of high sensitivity and sophistication in place, we have ventured into an era of observing and characterizing the atmospheres of exoplanets in greater detail. Based on mass and radius measurements, bulk densities are used to draw first conclusions about possible planetary chemical compositions: A rocky bulk composition of an Earth-like silicate/iron mixture appears consistent with masses and radii of short-period planets if their radius $<1.5R_{\rm Earth}$ (Dressing et al. 2015). For radii $>1.5R_{\rm Earth}$, bulk densities appear so low that most of these planets must have a large volatile atmosphere (Rogers 2015). The observation and characterization of these atmospheres could provide a unique opportunity to study the internal composition and surface material of rocky exoplanets (Miguel et al. 2011), which is largely unknown. Planetary atmospheres with local gas temperature >1000 K have a rich molecular chemistry, and they form silicate clouds similar to brown dwarfs (e.g. Sudarsky et al. 2005; Fortney et al. 2008; Witte, Helling & Hauschildt 2009). Clouds alter the observed spectra by flattening the ultraviolet (UV) and visible spectra due to scattering from small-sized particles, having a cooling effect on the atmosphere beneath the optically thick region by reflecting the received spectra and also by depleting the local gas phase of minerals to condense and form mineral cloud particles (Helling & Casewell 2014).

Even though it is crucial to provide a proper interpretation of observations, cloud formation processes in hot and warm super-Earth atmospheres are poorly studied. Clouds have been proposed for the super-Earth GJ436 b, wherein the observed spectrum in the range $1.2-1.6$ μm is featureless, indicating a possibility of a 'heavier than hydrogen' gas-phase molecular composition resulting in high-opacity clouds that form at a pressure altitude of $\sim 10^{-3}$ bars (Knutson et al. 2014). Fegley et al. (2016) study the surface outgassing of hot rocky exoplanets by taking into account the fractional vaporization by assuming that the gas contains the monomers that the rocks are made of. Schaefer, Lodders & Fegley (2012) and Schaefer & Fegley (2009) discuss the possible atmosphere of CoRoT-7b-like planets. They suggest the presence of Na and K clouds in the upper parts of the atmosphere. Miguel et al. (2011) explore the composition of initial planetary atmospheres of hot rocky super-Earths (HRSEs) in the *Kepler* planet candidate sample. Ito et al. (2015) conducted a similar study with a few more types of Earth rock compositions. Demory et al. (2016b) have derived a longitudinal temperature map of the super-Earth 55 Cancri e (55 Cnc e) and found a large temperature contrast of 1300 K between its day

★ E-mail: ch80@st-andrews.ac.uk

and night sides. Although they suggest the temperature map to be a surface map of the planet, Demory et al. (2016b) do not rule out the possibility of a dense atmosphere with thick clouds on the day side.

The aim of this paper is to explore cloud formation in hot and highly enriched exoplanet atmospheres. Atmospheres of small hot planets are poorly understood so that little is known about their composition, chemistry and condensibles. We therefore explore a diversity of scenarios, including extremes. Besides addressing specific objects (CoRoT-7b, 55 Cnc e), this strategy allows us to understand our results in a large context by comparing to known and better studied cases (like brown dwarfs that exhibit comparable thermodynamic properties to giant gas planets), and to identify trends regarding cloud properties and the effect of element abundances on cloud properties. We note for clarification that, for example, hydrogen-rich atmospheres for planets like CoRoT-7b and 55 Cnc e are unlikely, unless they are very young, as studied by Owen & Mohanty (2016). Lopez & Rice's (2016) fig. 1 suggests for a planet of $1.58 R_{\rm Earth}$ (CoRoT-7b's radius) that a percentage of H/He of less than 0.1 per cent remains in the atmosphere after 5 Gyr for all their highly irradiated cases.

Here we suggest that a rich, non-homogeneous cloud chemistry is to be expected for non-solar and for processed atmospheric element abundances as originating from evaporating planet surfaces or as a result of disc evolution (e.g. Helling et al. 2014; Cridland, Pudritz & Alessi 2016; Eistrup, Walsh & van Dishoeck 2016; Mordasini et al. 2016), which might lead to locally high metallicities in the gas being accreted by the planets. We explore the evaporating planet CoRoT-7b and the magma-planet 55 Cnc e for various Earth rock compositions as examples for possibly processed, non-solar element abundances. We compare these results with HD 149 026b, for which a 10 times solar metallicity in the element abundances was tested (Fortney et al. 2006), and use a standard solar element abundance for non-irradiated giant gas planet atmosphere as reference. We do not consider the physical processes that lead to planetary mass-loss, which we assume is launched above our computational domain. Intense X-ray and extreme ultra-violet irradiation (driving intense heating and ionization) in combination with centrifugal acceleration can lead to a hydrodynamic mass-loss from the upper atmospheres of hot Jupiters (Khodachenko et al. 2015). Tidal forces will decelerate a wind, and magnetohydrodynamic effects will confine the wind further to the volume of closed field lines (Trammell, Arras & Li 2011). Due to the complexity of the planetary mass-loss models, no consistent link has been made to the underlying atmosphere structure, where cloud formation affects the atmosphere structure and determines the observable spectrum, and the inner boundary is not well defined in these complex models. Section 2 describes our approach. We summarize our kinetic cloud formation model and the input properties used. We note that our model neither prescribed the number of seed particles, nor prescribed the particle size distributions (e.g. Helling & Fomins 2013). In Section 3, we investigate the gas-phase composition for different element abundances as a prerequisite for the clouds to form. Section 4 describes the cloud results obtained for different exoplanetary cases (CoRoT-7, 55 Cnc e, HD 149 026b, reference model) and the influence of different initial element abundances on the cloud structure. Section 5 contains our conclusions.

2 APPROACH

We apply our kinetic, non-equilibrium cloud formation model to investigate cloud structures in atmospheres of non-solar element abundances. We assess the impact of element abundances on the gas-phase chemistry and the cloud structure details for prescribed planetary atmosphere profiles.

2.1 Gas chemistry and kinetic cloud modelling

Gas-phase chemistry. We apply a chemical equilibrium approach to study the initial, undepleted gas composition for given atmospheric structures ($T_{\rm gas}$, $p_{\rm gas}$) and the various sets of element abundances described below. We use the code described in Bilger, Rimmer & Helling (2013). The cloud formation code contains a chemical equilibrium routine similar to Bilger et al. (2013) but without the large carbohydrate molecules.

Cloud formation model. Our cloud formation model describes the formation of clouds by nucleation, subsequent growth by chemical surface reactions on top of the seeds, evaporation, gravitational settling, element depletion/enrichment and convective replenishment (Woitke & Helling 2003, 2004; Helling & Woitke 2006; Helling, Woitke & Thi 2008b). The effect of nucleation, growth and evaporation on the remaining elements in the gas phase is fully accounted for (equations 10 in Helling et al. 2008b). The C/O ratio at the start of the cloud formation process is fixed at C/O = 0.5 for all of the initial cloud formation cases so as to be able to discern the differences in the chemistry due to varying silicate compositions. The surface growth of a diversity of materials causes the grains to grow to μm-sized particles of a mixed composition. We consider the reactions forming 12 different dust species (TiO_2[s], Al_2O_3[s], $CaTiO_3$[s], Fe_2O_3[s], FeS[s], FeO[s], Fe[s], SiO[s], SiO_2[s], MgO[s], $MgSiO_3$[s] and Mg_2SiO_4[s]) that react to form grain mantles of a mix of these species depending on the local gas density and temperature. The DRIFT model of Helling & Woitke (2006) used 60 growth reactions. We treat a total of 79 surface growth reactions in this paper, which are provided in Table A2. The seed formation is described by classical nucleation theory, which has been modified for TiO_2 nucleation to take into account the knowledge about $(TiO_2)_N$ cluster formation (Jeong, Winters & Sedlmayr 1999; Jeong et al. 2000; Lee et al. 2015a). A more extensive discussion of the theoretical background of seed formation is provided in section 3a in Helling & Fomins (2013). We note that photoionization may open reaction paths that enable the formation of complex molecules or clusters as precursers for seed formation at even lower temperatures and densities than considered here (Kirkby et al. 2011; Rimmer, Helling & Bilger 2014). Photochemistry is not part of our present cloud formation model.

2.2 Input properties

2.2.1 Element abundances

The element abundances are input properties that determine the gas-phase composition of the atmosphere and therefore also the cloud particle material composition. In this study, we consider the following species to model exoplanet atmospheres: H, He, Li, C, N, O, Fl, Ne, Na, Mg, Al, Si, S, Cl, K, Ca, Cr, Mn, Fe, Ni and Ti. The undepleted element abundances are called initial abundances ϵ_i^0. The close-in planets have an extremely hot surface that will melt forming a lava ocean that can vaporize, resulting in an enrichment of the initial composition of the atmosphere. Since the lava ocean composition for an exoplanet is poorly constrained, we adopt different potential compositions for a planetary crust, which will result in different elemental abundances for our enriched atmosphere. The

Table 1. Initial element abundances, ϵ_i^0, from magma compositions. Solar and meteorite abundances are shown for comparison.

Element abundance $\log(\epsilon_i/\epsilon_H)$	Komatiite[a]	BSE[b]	BSE[c]	MORB[c]	UC[d]	BC[d]	Solar[e]	Meteorite[e]
Si	7.54	7.54	7.54	7.54	7.54	7.54	7.54	7.55
O	8.09	8.10	8.10	7.97	8.00	7.97	8.69	8.43
Mg	7.52	7.62	7.64	7.01	6.61	6.29	7.54	7.56
Fe	6.86	6.72	6.72	6.68	6.51	6.34	7.45	7.49
Ca	6.63	6.48	6.46	6.42	6.59	6.30	6.36	6.33
Al	6.54	6.62	6.61	6.57	7.03	6.97	6.47	6.46
Na	5.82	5.71	5.73	5.69	6.53	6.52	6.33	6.30
Ti	5.12	5.01	5.06	5.66	5.49	5.39	5.02	4.95
K	4.93	4.56	4.47	4.79	6.12	6.27	5.08	5.11
Cr	–	–	5.36	4.62	–	–	5.64	5.67
P	–	–	4.12	4.77	4.79	4.82	5.36	5.44

Notes. [a]Schaefer & Fegley (2004), [b]O'Neill & Palme (1998), [c]McDonough & Sun (1995), [d]Taylor & McLennan (2009), and [e]Grevesse, Asplund & Sauval (2007).

enriched elements are O, Mg, Al, Si, Ca, Ti and Fe, and their initial abundances, ϵ_i^0, are adopted according to the different compositions for Earth planetary crusts tested in this paper: bulk crust (BC), upper crust (UC), MORB – metal-oxide-ridge basalt, BSE – bulk silicate Earth and komatite (see Table 1 and Section A1). All other elements are set to solar values initially, except if all elements are increased by the same factor. Our test cases remain hydrogen rich, unless we specifically test a decreased hydrogen content as in the case of 'BSE (low H)' ($10^{-5} n_H$). The cloud formation process changes the initial element abundances by nucleation, growth and evaporation with respect to those elements that are involved (O, Mg, Al, Si, S, Ca, Ti and Fe; see equations 4 and 8 in Woitke & Helling 2004).

Different sets of initial element abundances should influence the local temperature and pressure structure due to changing gas and cloud opacities. Differences in element abundances will also affect the mean molecular weight.

2.2.2 *Atmosphere profiles*

We utilize a pre-calculated thermodynamic structure of atmosphere models. The resulting limitation of our approach is therefore that changes of initial element abundances (Section 2.2.1) do not affect the (T_{gas}, p_{gas}) structure, nor will the forming cloud particles have an impact on the atmosphere structure considered. We note that the (non-irradiated) DRIFT–PHOENIX giant gas planet model and the models for HD 149026b, which we utilize in this paper, do include the radiative and chemical feedback of clouds on the atmosphere structure. The profile used for 55 Cnc e results from a retrieval approach and should therefore also mimic the presence of clouds in case they are present. We use the following planetary atmosphere profiles for our study of cloud formation in atmospheres with metal-enriched abundances:

(1) non-irradiated giant gas planet as reference and for comparison to previous works [DRIFT–PHOENIX model atmosphere: $T_{eff} = 2500$ K, $\log(g) = 3.0$];
(2) the metal-rich mini-giant planet HD 149 026b ($T_{eff} = 1757$K, $\log(g) = 3.23$; Fortney et al. 2006);
(3) CoRoT-7b as a hot super-Earth example with $T_{equ} = 2300$ K, $\log(g) = 3.62$, adopting the atmosphere model results from Ito et al. (2015);
(4) 55 Cnc e profile as an HRSE example adopting a retrieved profile ($T_{equ} = 2400$ K, $\log(g) = 3.33$; Demory et al. 2016a).

Fig. 1 compares these different types of atmosphere model structures. Note that different communities use different global temperature definitions.[1] The 1D (T_{gas}, p_{gas}) structures for 55Cnc e and HD 149 026b and that for the hot non-irradiated giant gas planet for $T_{eff} = 2500$ K, $\log(g) = 3.0$ populate the same part of the (T_{gas}, p_{gas}) diagram. The atmosphere profile that was suggested for CoRoT-7b by Ito et al. (2015) ($T_{equ} = 2300$ K) is far hotter than the gas-giant atmosphere profiles. The $T_{eff} = 2500$ K for the giant gas planet is chosen since it has a range of local gas temperatures similar to that of hot super-Earths or gas-giant planets that we wish to study. CoRoT-7b and 55 Cnc e receive a comparable amount of irradiating flux as they orbit similar stars at a similar distance. The

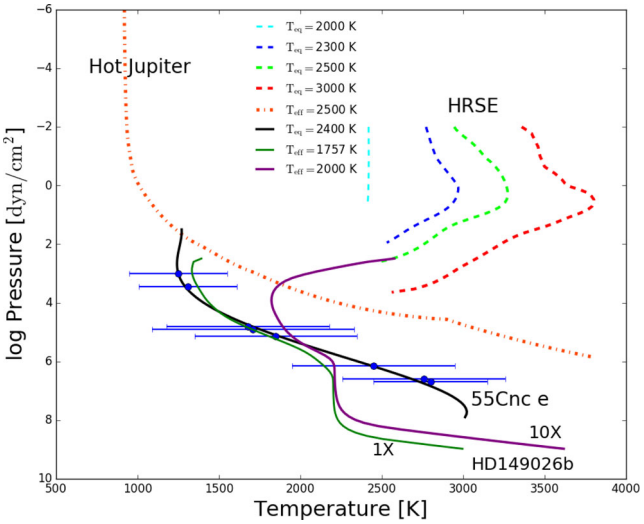

Figure 1. The (T_{gas}, p_{gas}) profiles of different planetary atmospheres. DRIFT–PHOENIX models with $T_{eff} = 2500$ K, $\log(g) = 3.0$ (orange dashed line; Witte et al. 2009, 2011). HRSE atmosphere profiles are demonstrated for $T_{eq} =$ 2000–3000 K (dashed light blue, blue, green and red lines; Ito et al. 2015); HD 149026b with 1× and 10× solar element abundances (solid purple and green; Fortney et al. 2006); and 55 Cnc e (solid black and blue points with error bars, Demory et al. 2016a).

[1] The sub-stellar point equilibrium temperature is given as

$$T_{eq}^4 = (1 - A_P)\frac{R_*^2}{D^2} T_*^4.$$

where R_* and T_* are, respectively, the radius and temperature of the host star, A_P is the planetary albedo and D is the orbital distance of the planet. The host star is assumed to emit blackbody radiation of 6000 K, and the magma composition is assumed to be BSE.

main differences between the two cases are therefore due to the different atmosphere profiles presently available in the literature and potential differences in their atmospheric compositions (55 Cnc e has a larger radius than CoRoT-7b, consistent with a more extended atmosphere). We have run our cloud formation model for all these model atmospheres with all element abundances listed in Table 1, but we will later confine our result presentation to a selected set of input atmosphere structures.

Giant gas planet. We use a DRIFT–PHOENIX model atmosphere with a surface gravity $\log(g) = 3.0$ and effective temperature $T_{\rm eff} = 2500$ K for our cloud formation study. Fig. 1 shows the atmospheric profiles of two different hot-Jupiters that are derived from the DRIFT-PHOENIX model atmosphere simulations described in Witte et al. (2009, 2011) for comparison. The atmospheric model used is in local thermal equilibrium, and the radiative and convective energy transport is solved to determine the local gas temperature. The local gas pressure is calculated assuming hydrostatic equilibrium, and the equations of state, opacity data and equilibrium chemistry calculations close this system of equations; see, for example, Helling & Casewell (2014).

Metal-rich mini-giant planets, for example, HD 149 026b: HD 149026b is an extrasolar giant planet with an orbit of 2.87 d around a metal-rich G0IV parent star. It has a radius of only $0.725R_{\rm J} \pm 0.05R_{\rm J}$ and a mass of $0.36M_{\rm J} \pm 0.03M_{\rm J}$ (114 $M_\oplus$; Sato et al. 2005). Evolution models suggest that the planet should have larger radii (Guillot et al. 1996), but it is decidedly small. Fortney et al. (2006) provide atmosphere models for the planet and suggest that a hot stratosphere (temperature inversion) may develop due to additional flux absorption by TiO and VO. The ($T_{\rm gas}$, $p_{\rm gas}$) profiles used in our study are shown in Fig. 1, where 1× (green) corresponds to solar abundance and 10× (purple) corresponds to a 10 times solar atmospheric profile. This model allows us to study the effect of an increase of element abundances by the same amount for each element compared to the solar element abundances.

Hot super-Earth CoRoT-7b (HRSE). We use ($T_{\rm gas}$, $p_{\rm gas}$) profiles from Ito et al. (2015) for an HRSE for a first assessment of cloud formation and their potential details for CoRoT-7b should cloud formation be possible. The atmosphere simulation by Ito et al. (2015) is a 1D plane-parallel thermal structure that is in radiative, hydrostatic and chemical equilibrium. These models use the ground pressure, $P_{\rm g}$, and molar fraction $x_{\rm A}$, which are functions of the ground temperature $T_{\rm g}$, which is determined assuming the magma ocean is a blackbody. No clouds are considered in these models. Fig. 1 shows several HRSE ($T_{\rm gas}$, $p_{\rm gas}$) profiles provided by Ito et al. (2015) for hot super-Earths with $T_{\rm eq}$ from 2000 to 3000 K. In the cases of $T_{\rm eq} \leq 2000$ K, the atmosphere is isothermal because the atmosphere is so optically thin that the ground is directly heated by the stellar irradiation (Ito et al. 2015). Ito et al. (2015) used $T_{\rm equ} = 2300$ K to represent CoRoT-7b.

Possible atmosphere on 55 Cnc e. 55 Cnc e is an interesting candidate to study the potential atmospheric compositions due to its mass and radius estimated at 8.09 ± 0.26 $M_\oplus$ (Nelson et al. 2014) and 2.17 ± 0.10 $R_\oplus$ (Gillon et al. 2012), which makes it fall into the category of a super-Earth. Given the extremely high equilibrium temperature ($T_{\rm eq} \sim 2400$ K) and its proximity to the parent star, it is highly likely that the planetary lithosphere is weak and most of the day-side surface of the planet will be in a semimolten or molten state, which would lead to magma oceans and possibly volcanic activity on the irradiated day side (Demory et al. 2016a).

Due to the high brightness of the host star, 55 Cnc e can be observed with great detail in the visible as well as the *Spitzer* 4.5-μm IRAC photometric band (Winn et al. 2011; Demory et al. 2012; Gillon et al. 2012). Based on the precise measurement of mass and radius alone, Demory et al. (2011) suggested a silicate-rich interior with a dense H_2O envelope of 20 per cent by mass, Gillon et al. (2012) suggested a purely silicate planet with no envelope, Madhusudhan (2012) suggested a carbon-rich planet with no envelope and Demory et al. (2016a) suggested an atmospheric model in which multiple volcanic plumes explain the large observed temperature variations on the day side. The ($T_{\rm gas}$, $p_{\rm gas}$) profile that we use in our study is derived from the figure in Demory et al. (2016a). This profile was retrieved based on the observed IRAC 4.5-μm brightness temperature ($T_{\rm B}$) between $T_{\rm min} = 1273^{-348}_{+271}$ K and $T_{\rm max} = 2816^{-368}_{+358}$ K. Such retrieved planetary atmospheres are therefore isothermal at the upper and the lower boundaries, in contrast to complete forward models like DRIFT–PHOENIX or those from Ito et al. (2015) and Fortney et al. (2006).

2.3 Atmospheric mixing

The vertical mixing is parametrized using the eddy diffusion coefficient K_{zz}, which represents the strength with which material can be transported into higher atmospheric layers (Agúndez et al. 2014). There has been extensive research on the choice of K_{zz} for the cases of hot-Jupiters (Moses et al. 2011; Miguel & Kaltenegger 2013; Parmentier, Showman & Lian 2013; Agúndez et al. 2014). Parmentier et al. (2013) use vertical diffusive coefficients determined by following passive tracers in their general circulation model. They adopt a K_{zz} (cm^2 s^{-1}) $= 5 \times 10^8$ p$^{-0.5}$ (bar) for HD 209458 b, which is a gas giant. Agúndez et al. (2014) used K_{zz} (cm^2 s^{-1}) $= 10^7$ p$^{-0.65}$ (bar) for the case of HD 189733 b and Miguel & Kaltenegger (2013) considered values between K_{zz} (cm^2 s^{-1}) $= 10^8$ and 10^9 for their atmospheric models of mini-Neptunes. We follow the approach detailed in Lee et al. (2015a) for the vertical mixing. The diffusion-mixing time-scale is derived from $\tau_{\rm mix} =$ constant $\times$ $H_{\rm p}^2/K_{zz}$ for a prescribed diffusion constant K_{zz}. A constant $K_{zz} = 10^{11}$ cm^2 s^{-1} was chosen for 55 Cnc e. Tests have shown that for the 55 Cnc e profile (black line joining blue dots with error bars in Fig. 1), cloud formation does not start for $K_{zz} < 10^9$ cm^2 s^{-1}. The K_{zz} value for HD 149026b is selected to be 10^{13} cm^2 s^{-1}. For CoRoT-7b, K_{zz} was varied between values ranging from 10^7 to 10^{15} cm^{2}s^{-1}.

3 RESULTS: EQUILIBRIUM GAS-PHASE COMPOSITION

Clouds form from an atmospheric gas if the appropriate thermodynamic conditions are met. Their composition depends on the chemical composition of the atmospheric gas. Witte et al. (2009) demonstrated how a (homogeneously) decreasing element abundance changes the cloud structure in brown-dwarf atmospheres by reducing the set of solar element abundances by the same factor from [M/H] = 0.0 to 6.0. Recent chemical modelling efforts in planet-forming discs show that planets will most likely form from a set of initial element abundances that is non-solar or from a simple scaling of the solar set of element abundances (Helling et al. 2014; Eistrup, Walsh & van Dishoeck 2016). In this section, we show the results and analyse the chemical gas-phase composition for all the cases explored in this paper. To keep the number of panels sensible, we chose only four sets of element abundances (solar, 10× solar, BSE and BSE with a low H abundance). We note that all figures will also contain results for extreme cases for completeness and for

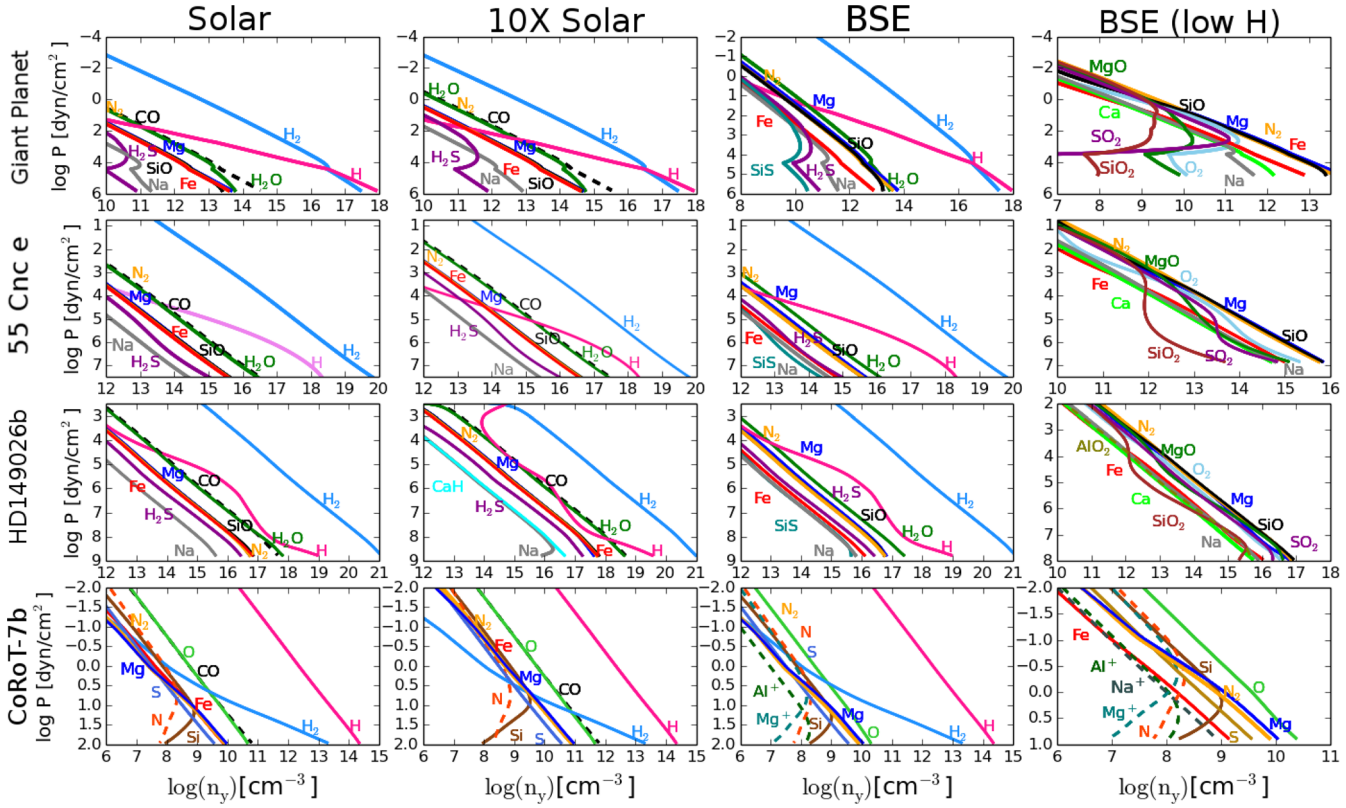

Figure 2. The gas-phase number densities, n_y (cm^{-3}), of the 10 most abundant gas species for four types of element abundances and four different ($T_{\rm gas}$, $p_{\rm gas}$) profiles. Different rows represent different atmospheric models as indicated, and the respective ($T_{\rm gas}$, $p_{\rm gas}$) profiles are shown in Fig. 1. The name of each gas species is indicated near the line with the same colour. Different columns represent different sets of initial element abundances: solar, 10× solar – 10× $\epsilon_{\rm solar}$ and BSE(low H) – BSE abundance with 10^{-5} × $\epsilon_{\rm H}$.

reference. These extreme cases are the hydrogen-rich atmospheres for 55 Cnc e and CoRoT-7b, which may be realistic only during a very short time of their infancy or when kicked back into a hydrogen-rich part of the planet-forming disc. The two BSE cases for the giant gas planet and HD 149026b can represent stages of a heavy influx of meteorites or even planetary collisions.

Fig. 2 shows the 10 most abundant species that result from our chemical equilibrium gas-phase calculations. In Figs 3–5, we show the results for the chemistry of one element at a time (Fig. 3: Si, Fig. 4: Mg and Fe, Fig. 5: Al and Ti). We generally observe that a lower hydrogen content [here: BSE (low H)] leads to higher abundances of oxides such as SiO_2, TiO_2, MgO, FeO and AlO_2H.

Giant gas planet. The atmosphere is dominated by volatiles for the solar, metal-enriched solar (10× solar) and BSE cases. In the case of solar abundance, the atmosphere is primarily composed of H_2, H and CO, as shown in Fig. 2. Increasing the element abundances homogeneously results in an increase of the molecular number densities (compare the first and second columns in Figs 3–5). This effect is stronger for Mg, Si and Fe than for elements with an intrinsically lower abundance like Ti and Al.

The BSE atmosphere has an increase in H_2O, SiO, SiS, K, Al and TiO, among others (see Fig. 2). The differences in the solar and BSE abundances with a fixed C/O ratio of 0.5 are quite pronounced in the higher pressure regions where the amount of TiO and TiO_2 increases slightly with a drastic decrease in TiC molecules in the BSE case. An increase in such UV absorbers may therefore induce a local temperature inversion (Fortney et al. 2006). The strongest changes with metallicity occur for the Mg-binding species.

55Cnc e. The atomic species dominate the gas phase for all elements in the case of BSE composition. Tsiaras et al. (2015) in their analysis of an atmosphere around 55 Cnc e show that the abundances of HCN and C_2H_2 increase while the abundance of H_2O decreases drastically, which is similar to the results that we obtain for a test BSE composition with C/O = 1.0 (not shown) as compared to an oxygen-rich solar abundance.

Metal-rich mini-giant planets, for example, HD 149026b. The third rows of Figs 3–5 show the gas-phase composition for HD 149026b. The temperature inversion is seen at around 2700 K, where all the gases go through a sudden increase in concentration. The second panel of the third row for the figures shows the plot for an enriched atmosphere with 10× the solar metallicity. The abundance of oxides of Ti, Al, Fe, Mg and Si is higher for HD 149026b as compared to other planets, which would add to the cloud opacity by imposing strong cloud particle growth.

Hot super-Earth CoRoT-7b. The fourth row of Figs 3–5 shows the number densities of the dominating species for the CoRoT-7b case. The local gas temperatures for this planet are considerably higher compared to the other three planetary model atmospheres due to the stronger irradiation and the high-temperature profiles adopted from Ito et al. (2015). The atmospheric model of CoRoT-7b is representative of a rocky planet. Due to the closeness to its host star and high irradiation, the volatiles might have escaped. Therefore, we would expect the BSE case with a low hydrogen content to be the most representative of CoRoT-7b initial element abundances. A comparison of the BSE case with the solar element abundances

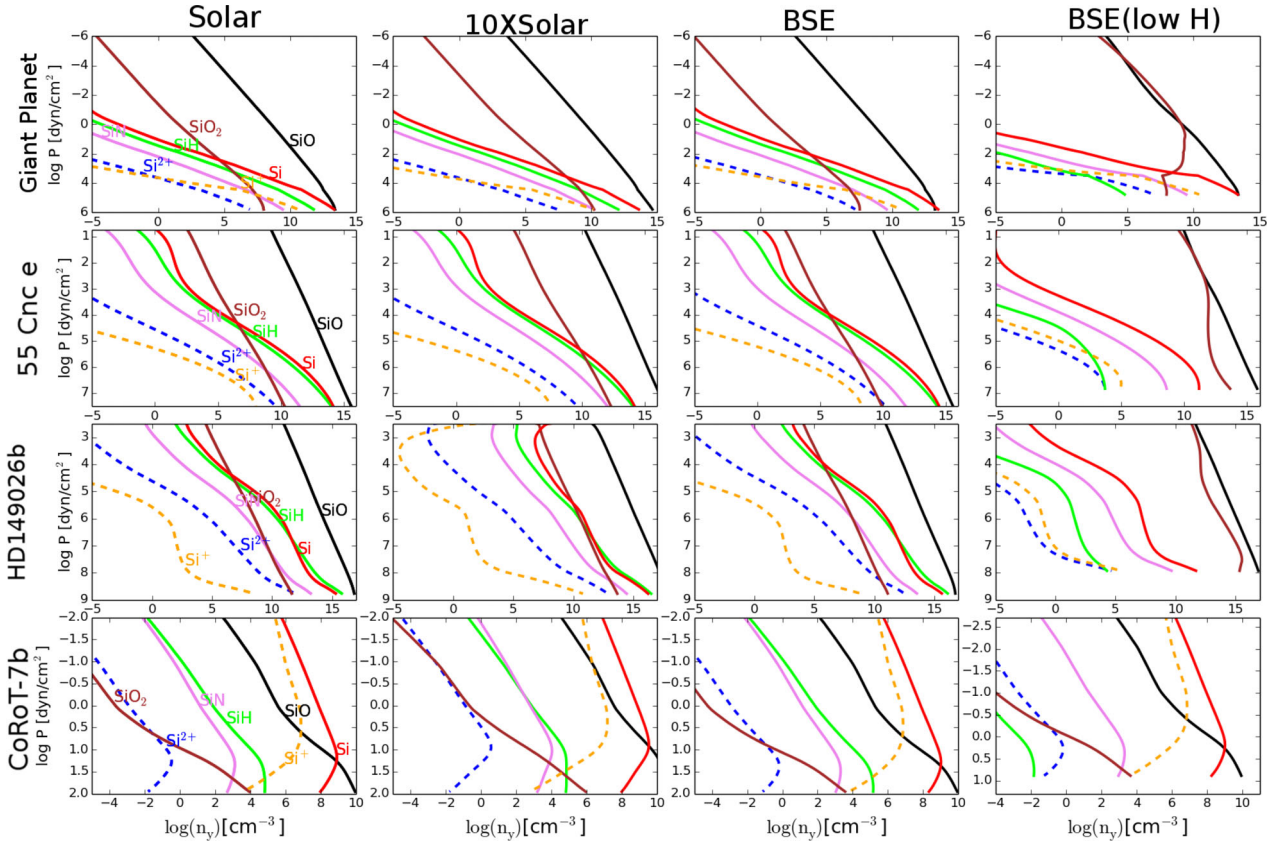

Figure 3. The gas-phase number densities, n_y (cm^{-3}), for Si-binding species in chemical equilibrium for four types of elements abundances and four different (T_{gas}, p_{gas}) profiles. Different rows represent different atmospheric models as indicated, and the respective (T_{gas}, p_{gas}) profiles are shown in Fig. 1. Different columns represent different sets of element abundances: 10× solar – 10× ϵ_{solar} and BSE(low H) – BSE abundance with 10^{-5} × ϵ_H. All species have the same line colour in all panels and are provided in the first column.

shows the sensitivity of the gas composition to uncertainties in initial element abundances. We note that a changing hydrogen content will affect the mean molecular weight of the whole atmosphere.

The atmosphere of CoRoT–7b is primarily composed of gases in their atomic and ionic states; hydrogen is present as H (see Fig. 2). Si species such as SiO and SiS are still quite dominant. We find most of the other elements such as Ti, Mg, Fe and Al to be dominant in their atomic and ionic states in both solar and BSE atmospheres. SiO dominates the Si-binding gas species at high gas pressures, followed by Si and Si^+. This hierarchy is somewhat metallicity-dependent. Mg, Fe, Al and Ti appear always in their atomic states followed by their singly ionized state (Mg/Mg^+, Fe/Fe^+, Al/Al^+ and Ti/Ti^+). Al^+ and Ti^+ appear at lower pressures than Mg^+ or Fe^+ for the CoRoT-7b profile utilized here. Therefore, the atmosphere of CoRoT-7b is strongly ionized on its day side. This suggests that either no cloud formation can take place or other cloud formation paths than those considered here need to be considered. For example, noctilucent clouds on Earth are suggested to form through ion–cluster nucleation.

A decreasing hydrogen abundance does not affect these results significantly with respect to the most abundant species of each element.

3.1 Summary

We have analysed the gas-phase composition for different sets of initial abundances as a starting point for cloud formation. The primary abundant species is H_2 in all of our atmospheres except that of CoRoT-7b, which has atomic H as the dominating species due to its higher gas temperatures. The BSE atmosphere model used for CoRoT-7b suggests the presence of gases such as SiO, Mg, K, Na and O, which are also found in the atmospheres of 55 Cnc e and HD 149026b. SiO is the dominant gas resulting from Si in all of the planet cases except CoRoT-7b, where atomic Si is the dominant gas-phase species due to higher local gas temperatures (except at high gas pressures). It is followed by SiO_2 in the upper parts of the atmospheres for the gas giants 55 Cnc e and HD 149026b.

Atomic Fe is the dominant species among the Fe-binding gas-phase species, for all of the planets and element compositions considered here. Similarly, atomic Mg is the dominant species among all of the Mg-bearing gas-phase molecules, except for HD 149026b with BSE (low H), where we see MgO as another dominant species. However, giant planets with low hydrogen content are an extreme and most likely unrealistic case. Our results suggest that the chemical gas-phase composition does not change drastically if the element abundances are increased by the same factor for all elements starting from solar composition (up-scaled solar composition), but it leads to higher gas-phase concentrations of enriched elements (as can be seen in the second column of Figs 3–5). We note that our gas-phase results for CoRoT-7b so far suggest that the atmosphere is highly ionized and the plasma process may therefore affect the atmosphere (Helling et al. 2016a).

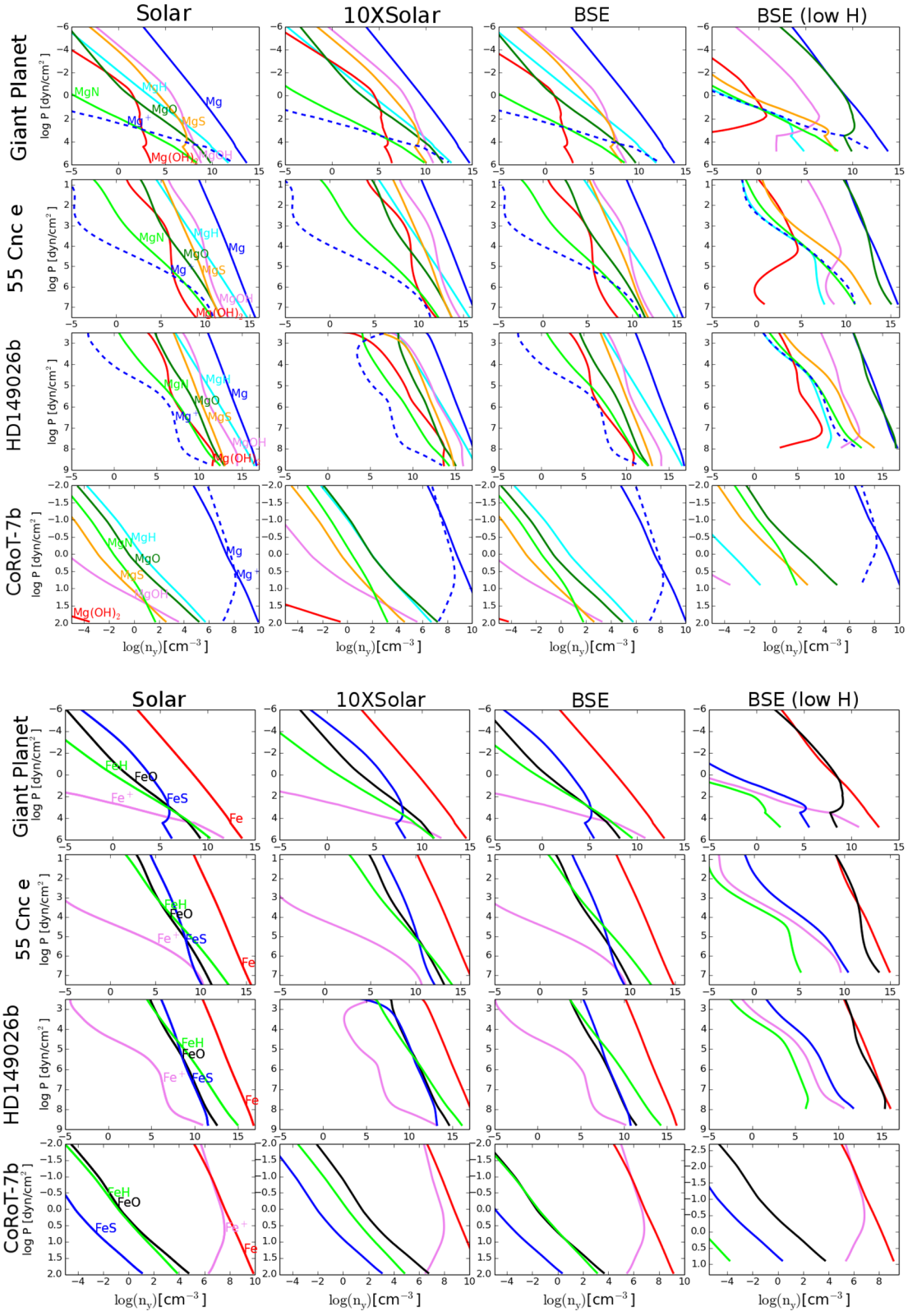

Figure 4. Same as Fig. 3 but for Mg-binding (top panel) and Fe-binding (bottom panel) gas-phase species.

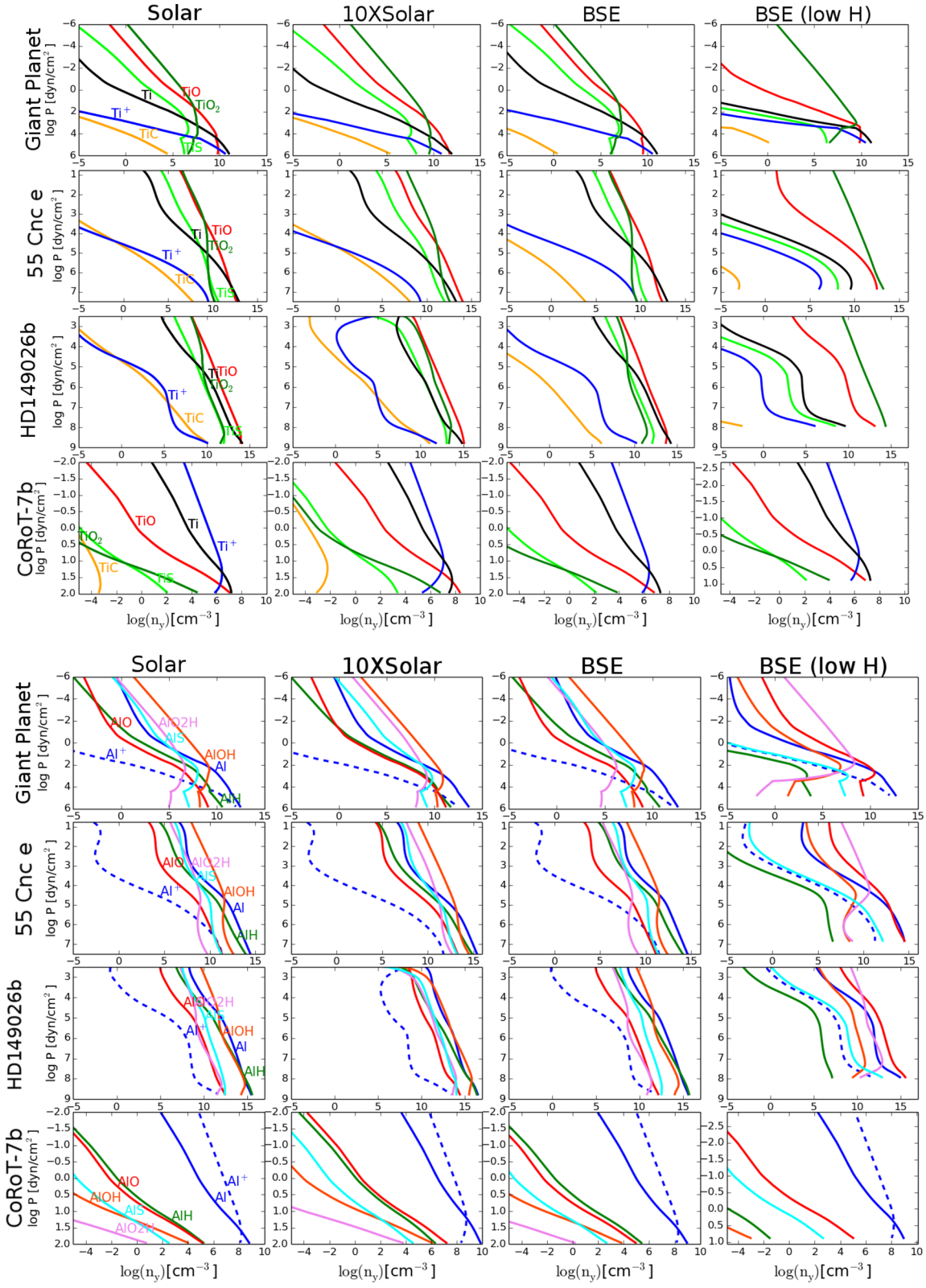

Figure 5. Same as Fig. 3 but for Ti-binding (top panel) and Al-binding (bottom panel) gas-phase species.

Table 2. Global parameters of the planets considered in this paper.

Planets	a (au)	$T_{\rm global}$ (K)	M (M⊕)	$\log(g)$ (cm s^{-2})	References
Giant gas planet	–	$T_{\rm eff} = 2500$	–	3.0	Witte et al. (2009)
55 Cnc e	∼0.015	$T_{\rm equ} = 2400$	8.63	3.33	Demory et al. (2016a)
HD 149 026b	∼0.042	$T_{\rm eff} \sim 1800$	114	3.23	Fortney et al. (2006)
CoRoT-7b	∼0.017	$T_{\rm emu} = 2300$	<9	∼3.5	Ito et al. (2015)

4 CLOUDS IN ATMOSPHERES OF NON-SOLAR ELEMENT ABUNDANCES

Table 2 summarizes the global parameters of the planets that we use to evaluate cloud structures for planets that have been suggested to possess potentially non-solar sets of initial element abundances.

Figs 6, 8 and 10 show the input ($T_{\rm gas}$, $p_{\rm gas}$, $\tau_{\rm mix}$) in the top panel. The second, third and fourth panels demonstrate the governing cloud variables [nucleation rate J_* (cm^{-3} s^{-1}), net growth velocity $\chi_{\rm net}$ (cm s^{-1}) and equilibrium drift velocity $v_{\rm dr}$ (cm s^{-1})] and resulting cloud properties [cloud number density $n_{\rm d}$ (cm^{-3}), mean cloud particle size $\langle a \rangle$ (μm) and dust-to-gas ratio $\rho_{\rm d}/\rho_{\rm gas}$] for five sets of element abundances (BSE, BC, UC, MORB and solar). The fifth, sixth and seventh panels present the results only for the set of solar element abundances but now detailed for the 12 individual growth materials involved (see Section 2.1): net growth velocity $\chi^s_{\rm net}$ (cm s^{-1}) for material s, volume fraction $V_s/V_{\rm tot}$ for material s and the effective supersaturation ration $S_{\rm eff}$ for each material. Figs 7, 9 and 11 contain four groups of three panels that are similar to the fifth, sixth and seventh panels in Figs 6, 8 and 10 but for the remaining sets of element abundances (BSE, UC, BC and MORB).

4.1 Clouds that form in the atmosphere of a giant gas planet

Fig. 6 shows how the cloud properties and, hence, the cloud structure changes in the case of different sets of initial element abundances for a sample atmosphere representative of a non-irradiated gas giant [$T_{\rm eff} = 2500$ K, $\log(g) = 3.0$] being representative for a long-period or free-floating planet.

The nucleation rates (J_*, second panel, left-hand side) appear similar for the sets of element abundances; however, BC abundance causes a less efficient nucleation at the nucleation peak. BC further allows the nucleation to spread somewhat more towards higher temperatures and higher gas pressure than any of the other sets of element abundances. The net growth velocity ($\chi_{\rm net}$, second panel, right-hand side) reaches largest values for solar abundance. There is significant variation in the final particle sizes ($\langle a \rangle$, third panel, left-hand side) before the cloud particles evaporate. The particles for the BSE set of initial element abundances reach the biggest sizes followed by the BC, solar and then MORB and UC abundance sets. This is a clear hierarchy of available gas-phase growth species rather than an effect of the local gas temperature because no detailed feedback on to the gas temperature is taken into account in this work based on the new cloud structures derived here. The underlying model atmospheres from DRIFT–PHOENIX and from Fortney et al. (2006) do include the effect of clouds on the temperature structure and element abundances. This is also seen from the drift velocities (v_{dr}, third panel, right-hand side) with BSE particles being the biggest and having the largest drift velocity. The individual material volume fractions ($V_s/V_{\rm tot}$, sixth panel) reflect the individual net growth velocities ($\chi^s_{\rm net}$, fifth panel) of each of the materials, s, and demonstrate where growth is most efficient for which material. The composition for the solar set of element abundances is dominated by TiO_2[s] seed formation in the upper atmosphere. Other dust species start to condense on the seed, decreasing its volume fraction steadily. A large fraction of the cloud layer is dominated by Mg/Si/O-containing materials, and below that (i.e. at higher temperatures) Al- and Fe-containing species occupy a larger volume fraction by forming predominantly Al_2O_3[s] and Fe[s] until the particles become thermally unstable and evaporate completely. More details can be found in earlier publications (e.g. Helling et al. 2008b; Helling & Casewell 2014; Lee et al. 2015b; Helling et al. 2016b).

Fig. 7 provides details about the variation of material composition of the cloud particles for non-solar sets of element abundances. We see an atmosphere with BSE composition to be consisting of Mg-binding materials (∼30 per cent) and Si-binding materials (∼40 per cent), and, finally, Al_2O_3[s] dominates as the primary dust species until a pressure of 10^3 dyn cm^{-2} before the particles evaporate. The atmospheres with a BC, UC and MORB type of compositions have significant differences as compared to BSE, with the cloud particles being primarily composed of SiO[s] and SiO_2[s], which in a combined manner constitute more than 80 per cent of the cloud volume fractions in each case. Hence, objects with a MORB-type (or UC/BC) set of initial element abundances can be expected to have mineral clouds predominantly made up of Si–O cloud particles with smaller impurities from high-temperature condensates.

4.2 Clouds that form in the atmosphere of the metal-rich giant gas planet HD 149 026b

HD 149 026b can be classified as a mini-giant planet with a mass of 114 M⊕. Fortney et al. (2006) investigate the atmospheric and cloud properties for the planet with varying metallicities, such as [M/H] of 1×, 3× and 10× with TiO and VO enrichment of 3× and 10×. We perform our cloud modelling on a similar ($T_{\rm gas}$, $p_{\rm gas}$) profile for 1× solar abundance, as shown in Fig. 1, while varying the silicate abundances according to our four different Earth silicate compositions of BSE, BC, MORB and UC. Our models suggest a high value of vertical mixing with $K_{zz} = 10^{13}$ cm^2 s^{-1} or higher is needed for the atmosphere to be able to form dust clouds.

Figs 8 and 9 show the dust cloud properties for HD 149 026b as a result of our kinetic cloud formation model. Also here, the cloud formation is triggered by the occurrence of TiO_2 nucleation. Similar to previous findings or the giant gas planet atmosphere model, the nucleation rates ($J^\star$, second panel, left-hand side) differ by one to two orders of magnitude for the different sets of non-solar element abundances. The MORB composition produces the highest nucleation due to its higher Ti abundance (see Table 1). The particle growth velocities are the highest for a solar composition, and the particles reach the largest sizes (∼3 μm) followed by a BSE composition. The drift velocities ($\langle v_{\rm dr} \rangle$) are found to be in the same sequence of solar followed by BSE, MORB, BC and UC, respectively. The particles formed from a solar composition gas are thermally stable in a larger range of pressure before they evaporate

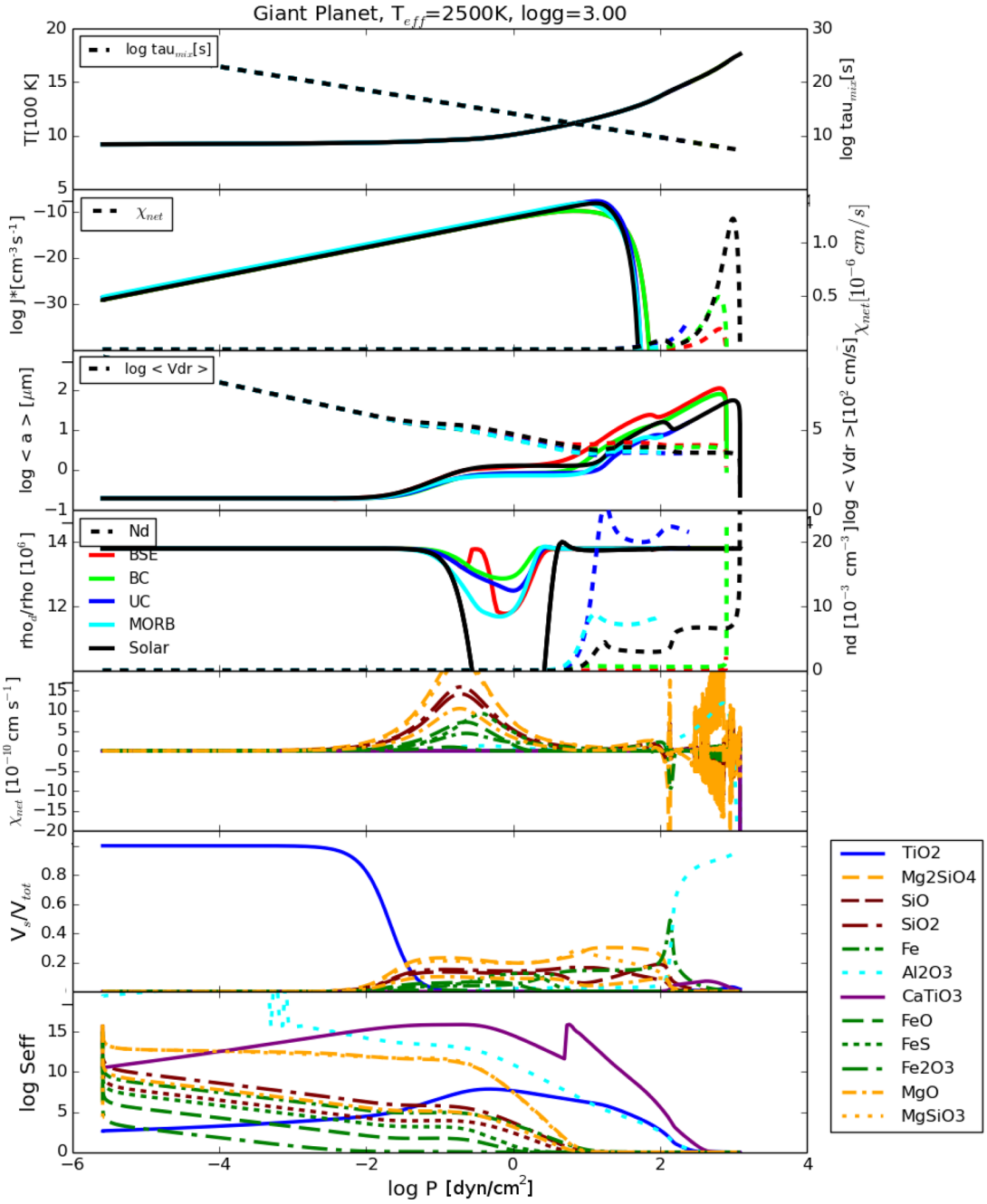

Figure 6. Cloud structure and cloud details for a giant gas planet [$T_{\rm eff}$ = 2500K, log(g) = 3.0] DRIFT–PHOENIX atmosphere model. **First panel:** local gas temperature, $T_{\rm gas}$ (solid line), and mixing time-scale $\tau_{\rm mix}$ (dashed line); **Second panel:** nucleation rate, log J_* (solid line), and dust growth velocity, $\chi_{\rm net}$; **Third panel:** mean cloud particle size, log $\langle a \rangle$, and drift velocity, log $\langle v_{\rm dr} \rangle$; and **Fourth panel:** dust-to-gas mass ratio, $\rho_{\rm d}/\rho_{\rm gas}$, and particle number density, $n_{\rm d}$. The cloud properties based on five sets of initial element abundances (solar – black, BSE – red, BC – green, UC – blue and MORB – sky blue) are shown in different colours in the second, third and fourth panels. The **Fifth** and **Sixth panels** are for solar element abundances only, and the results are detailed for the 12 different growth species s; **Fifth panel:** grain growth velocity, χ_s; and **Sixth panel:** material volume fraction, $V_{\rm s}/V_{\rm tot}$. The **Seventh panel** shows the effective supersaturation ratio, log $S_{\rm eff}$.

completely. The dust number densities ($n_{\rm d}$) are the highest for a MORB composition, again as a consequence of the highest J_*.

A solar and BSE composition in HD 149026b follows a similar trend of dust composition, wherein, just after the nucleation, Mg-binding silicates dominate the dust volume fraction with ∼40 per cent of the dust having Mg-binding dust species and is followed by Si-binding (∼40 per cent) and Fe-binding (∼30 per cent) species, which dominate the cloud base. For BC, UC and MORB compositions, our models suggest that the cloud particles are mainly made up of Si-binding species (∼60 per cent) and the cloud base having an increased amount of Al_2O_3[s], which increases up to ∼40 per cent at the cloud base. Table 3 shows the average volume fractions for each of the dust-forming species on three of the possible atmospheres. Fortney et al. (2006) consider atmospheric inversions due to the presence of TiO in their models, but our dust cloud models suggest an upper atmosphere in which TiO is heavily

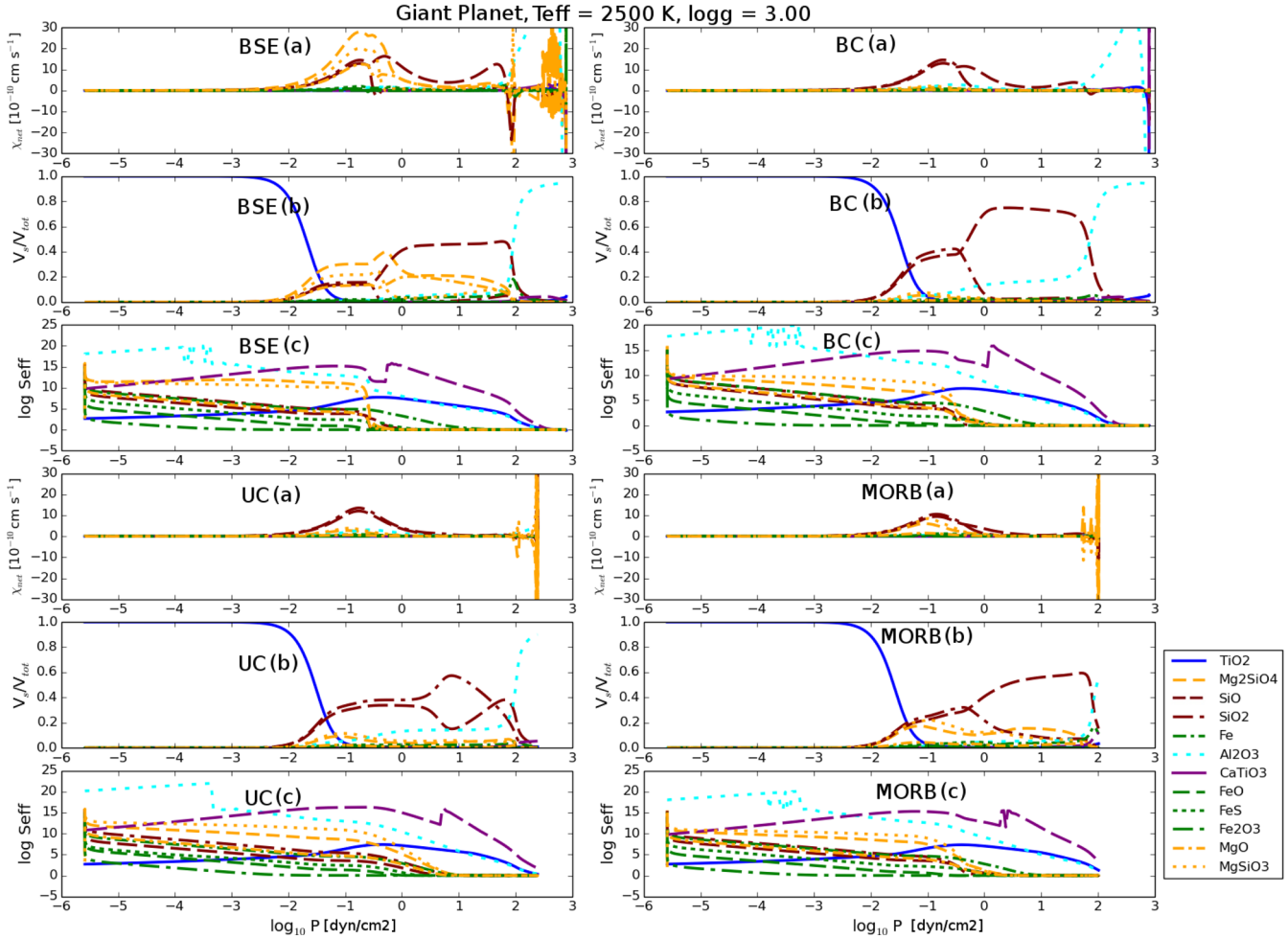

Figure 7. The cloud particle property results for a giant gas planet [$T_{\rm eff}$ = 2500 K, log(g) = 3.0] DRIFT–PHOENIX atmosphere model for four different sets of initial element abundances in detail for the 12 different growth species s: (a) grain growth velocity, $\chi_{\rm s}$ (cm s^{-1}); (b) material volume fraction, $V_{\rm s}/V_{\rm tot}$ (per cent); and (c) effective supersaturation ratio, log $S_{\rm eff}$. The four compositions BSE, BC, UC and MORB have been labelled on each plot.

depleted due to the seed formation. This is not a new finding and has been demonstrated for many cases (e.g. Helling et al. 2008b; Witte et al. 2009; Lee et al. 2015b). Such an element depletion would result in a loss of temperature inversion or suppression of the inversion zone to lower parts of the atmosphere where the TiO density is higher.

The cloud structure for HD 149026b is comparable to the results for the hot giant gas planet (Section 4.1), but the cloud reaches considerably deeper into the atmosphere.

4.3 Clouds in the atmosphere of 55 Cnc e

Figs 10 and 11 show the cloud properties for 55 Cnc e. Cloud formation occurs only in a thin atmospheric region near the top of the adopted ($T_{\rm gas}$, $p_{\rm gas}$) profile, where the local gas temperature and densities allow seed formation and efficient subsequent particle growth (compare pressure intervals in Figs 1 and 10). The extension of the cloud layer in the atmosphere of 55 Cnc e is therefore considerably smaller compared to the other cases studied here.

TiO_2 nucleation occurs throughout the whole atmosphere domain available for 55 Cnc e. Seed formation (J_*, second panel, left-hand side) differs by about one order of magnitude for the different sets of element compositions, which affects the number of cloud particles formed accordingly. The MORB composition attains the highest nucleation rates, which can be attributed to its higher abundance of Ti molecules leading to efficient nucleation. The sets of solar and BC element abundances result in the least efficient nucleation rate; hence, fewer cloud particles, $n_{\rm d}$, are formed. The growth velocities (second panel) are the highest for a solar composition followed by BSE, BC, UC and MORB. The particles encounter denser regions as they settle gravitationally and, thereby, also increase their size in the process due to the availability of more reaction material. In the case of 55 Cnc e, we observe a smooth change with height of the cloud material composition, which is due to the fact that the cloud layer is thin as compared to the cloud layer in the gas giant. This, however, may be a bias due to the domain of the prescribed atmosphere model available. The solar and BSE compositions have Mg-binding silicates (∼25 per cent) for the most part of the dust cloud, and it further increases to ∼30 per cent of the dust before evaporation. Si-containing growth species SiO and SiO_2 constitute ∼15 per cent of the cloud particles. Fe, Al and Ca species are present in minority (<5 per cent) in the BSE atmosphere. SiO and SiO_2 form the majority of the dust particles for the BC, UC and MORB atmospheres, which is due to the lower Mg content available to condense on the dust particles.

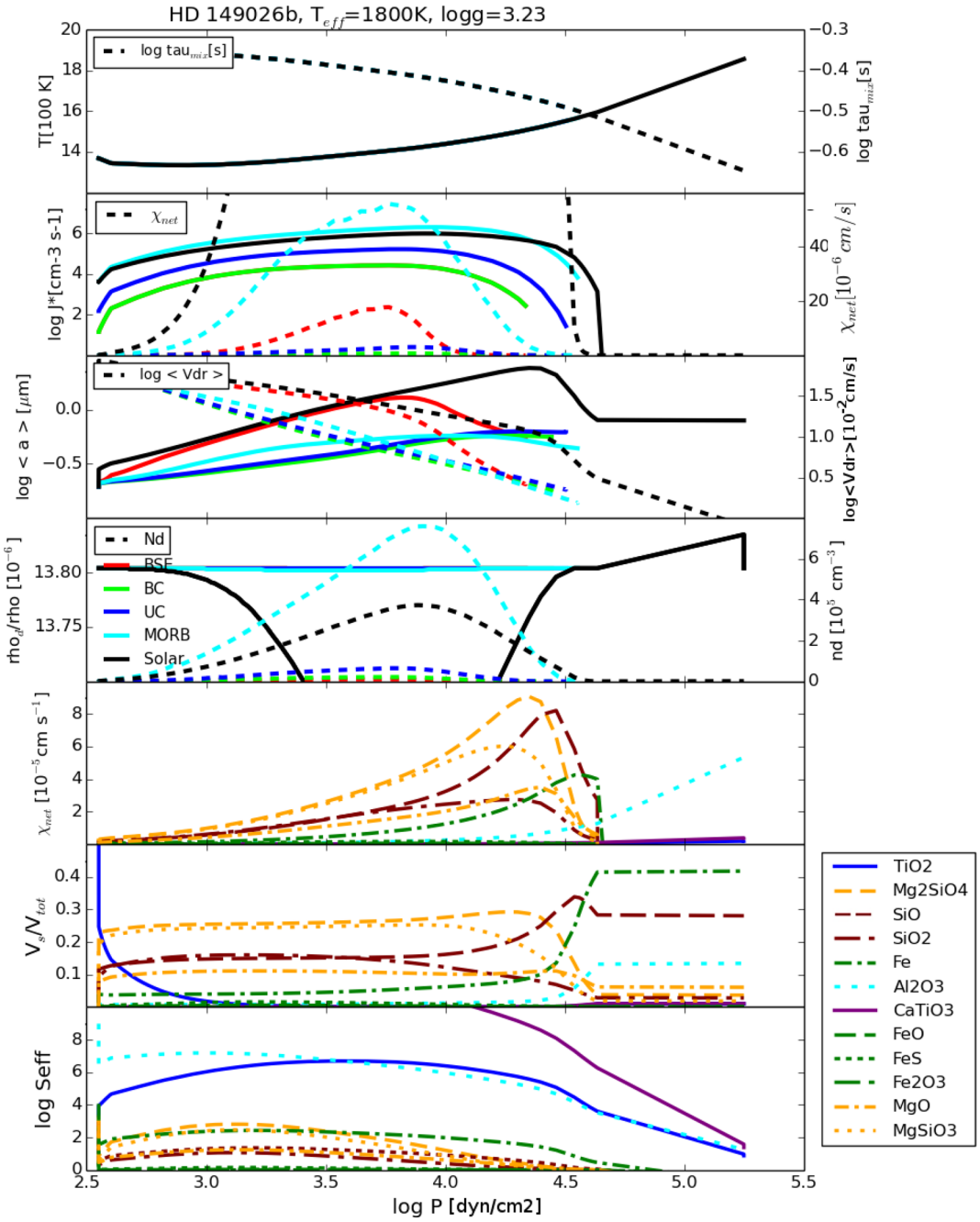

Figure 8. Cloud structure and cloud details for HD 149026b [$T_{\rm eff}$ = 1757 K, log(g) = 3.23] for five sets of initial element abundances (second, third and fourth panels). The figure has the same structure as Fig. 6.

Our results for 55 Cnc e demonstrate how sensible cloud formation reacts on the initial set of element abundances: Solar abundances disfavour an efficient seed formation (based on TiO_2) but allow for the most efficient surface growth processes among the sets of element abundances studied here. In contrast, BC also disfavours efficient nucleation, but it also slows down surface growth, being the least efficient in the sets studied. Consequently, the solar case produces clouds with a few but big particles, which rapidly rain out, and the cloud particles forming based on other sets remain suspended in the atmosphere for longer due to their smaller sizes.

4.4 The possibility of clouds in the atmosphere of CoRoT-7b

CoRoT-7b is an interesting candidate to analyse the possibility of cloud formation due to its extremely high local gas temperatures (>2500 K) and low local gas pressures [$-2 < \log(p_{\rm gas}) < 2$ (dyn cm^{-2})], making it a challenging candidate for cloud formation based on the presently available ($T_{\rm gas}, p_{\rm gas}$) structures. Fig. 1 demonstrates the large differences between those atmospheres where we have shown that clouds form and the atmosphere structures proposed for HRSE objects like CoRoT-7b. We investigated if cloud formation is possible on CoRoT-7b's day side by using the sample atmosphere profiles for a rocky planet with four different $T_{\rm eq}$

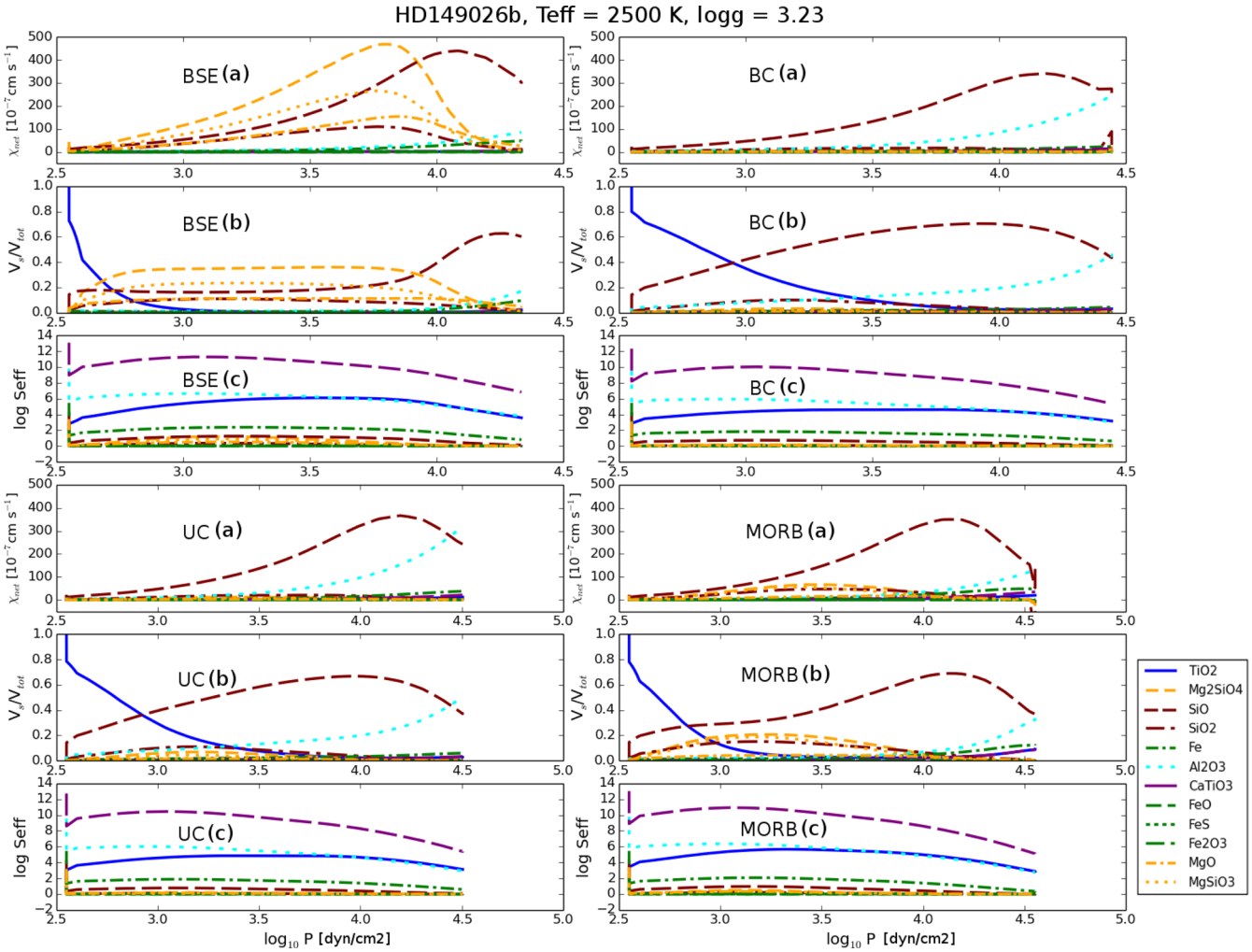

Figure 9. Same as Fig. 7 but for HD 149026b [$T_{\rm eff}$ = 1757 K,log(g) = 3.23].

(Fig. 1). Our kinetic cloud model does not suggest any cloud formation on the day side of CoRoT-7b for the atmosphere structures provided. Our finding, however, does not preclude cloud formation on the night side.

Schaefer & Fegley (2009) predict clouds of Na and K in the planet's atmosphere based on their phase-equilibrium approach. However, Gao & Benneke (2016) show that it cannot be taken for granted that such species actually nucleate, and the argument that has been put forward in Helling & Fomins (2013). Phase-equilibrium approaches focus on possible end-results of condensation processes but do not offer insight into the process of formation (Helling et al. 2008a). The ($T_{\rm gas}$, $p_{\rm gas}$) structures utilized here for CoRoT-7b appear hot enough that a strong ionization of the atmospheric gas should be expected according to our gas-phase composition study in Section 3. Given the high irradiation on to an existing atmosphere, strong winds will develop and transport ionized gas into cooler atmospheric regions where clouds will form similar to 55 Cnc e. The night-side/day-side transition region will most likely be electrostatically active, and electric currents are likely to affect the weather on CoRoT 7b, as suggested in, for example, the review by Helling et al. (2016b).

4.5 Summary

Table 3 provides an overview of global changes of the cloud structure depending on the sets of initial element abundances. We chose to visualize this in terms of volume fractions [$V_s/V_{\rm tot}$ (per cent)] at three typical heights inside the cloud, the maximum nucleation rate and the average mean grain size throughout the 1D cloud layer. These values can serve as guidance for retrieval methods.

The highlighted values for $V_s/V_{\rm tot}$ that several materials dominate the cloud particle composition, but the type of material changes with height was studied in all cases. Table 3 further demonstrates that a number of materials do contribute with less than 10 per cent to the overall cloud particle volume ($CaTiO_3$[s], Fe_2O_3[s], FeS[s] and FeO[s]).

The nucleation species TiO_2[s] dominates the cloud particle composition at the cloud top, while Mg–Si–O materials provide the material bulk independent of the set of initial element abundances.

We use the maximum nucleation rate and the average mean grain size as measured to compare our results for the individual objects (hot gas giant, HD 149026b and 55 Cnc e). This clearly shows that the effects of the different initial element abundances are negligible compared to differences in local thermodynamic conditions. The

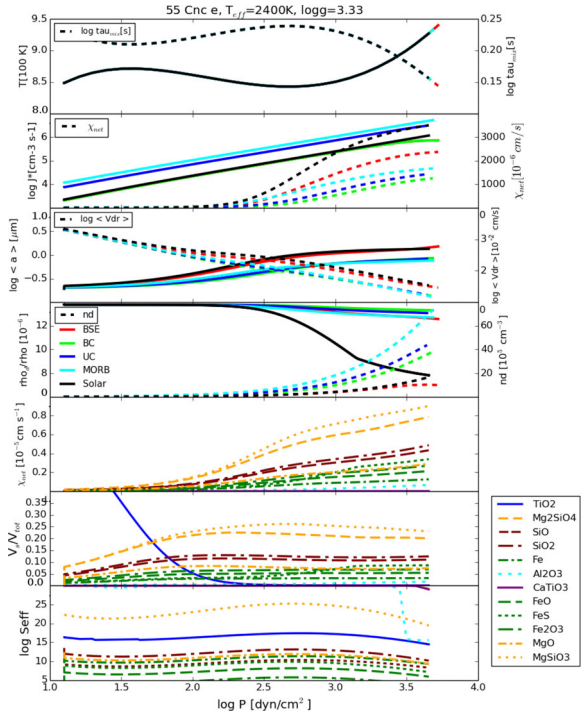

Figure 10. Cloud structure and cloud details for 55 Cnc e [$T_{\rm eff} = 2400$ K, $\log(g) = 3.33$] for five sets of initial element abundances (second, third and fourth panels). The figure has the same structure as Fig. 6.

anticorrelation between nucleation rate (hence, number of cloud particles formed) and mean grain size outlined earlier also prevails globally.

CoRoT-7b has no clouds forming on its day side and a strong day-side/night-side contrast should therefore be expected, which is determined by the planet's cloud formation.

5 CONCLUSIONS

Element abundances are important input properties for atmosphere (and evolutionary) modelling, which are, however, rarely known. Determining element abundances for extrasolar planets would be a valuable exercise as this might allow us to back-trace their place inside a planet-forming disc. However, chemical processing inside the protoplanetary disc and in the planet's atmosphere needs to be known well enough for this exercise.

This work is the first attempt to model cloud formation in planetary atmospheres with Earth-silicate-like element compositions. Our equilibrium chemistry gas-phase composition reflects the adopted silicate element compositions from the rocky and the solar element abundances. Apart from the volatile rich atmosphere consisting primarily of H_2, H and CO, there is an increase in content of gases such as Mg, Fe, SiS, Al, Ca, Si, Ti and K.

Our results suggest that clouds form in the atmospheres of 55 Cnc e, HD 149 026b and also in the hot gas giant, as we demonstrated in previous works. Cloud formation in atmospheres of evaporating magma planets (referring to planets with a molten surface) like 55 Cnc e requires a vertical recirculation of condensible material of $>10^{11}$ cm^2 s^{-1}. Vertical replenishment mechanisms have not been explored in detail in this work, but a large day–night temperature gradient may favour a circulation mechanism and hence

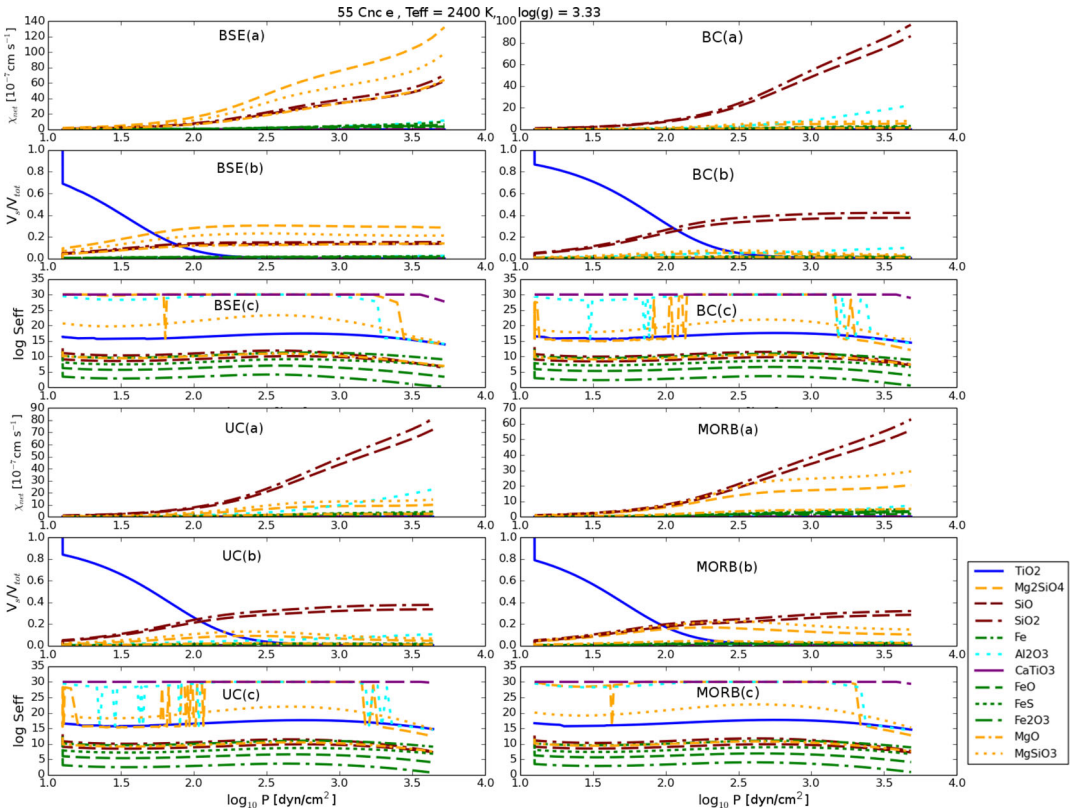

Figure 11. Same as Fig. 7 but for 55 Cnc e [$T_{\rm eff} = 2400$ K, $\log(g) = 3.33$].

Table 3. A comparison of characteristic cloud properties for a gas giant, 55 Cnc e and HD 149026b: the volume fractions [$V_s/V_{\rm tot}$ (per cent)] for individual materials s, the maximum nucleation rates [$\log_{10}J_{*,\,\rm max}$ (cm^{-3} s^{-1})] and cloud-averaged mean cloud particle radius [$\langle a\rangle_{\rm avg}$ (μm)] for three types of compositions. The cloud properties are compared for the cloud top, the middle (approximate half-length of the cloud) and for the cloud base (where the cloud particles have evaporated). All $V_s/V_{\rm tot} > 10$ per cent cases are shown in boldface.

Volume fraction $V_s/V_{\rm tot}$ (per cent)	$\epsilon_{\rm i}^0$	Gas giant			55 Cnc e			HD 149026b		
		Cloud top	Middle	Base	Cloud top	Middle	Base	Cloud top	Middle	Base
$p_{\rm gas}$ [bar]		$10^{-5.5}$	$10^{1.3}$	10^{3}	$10^{6.04}$	$10^{6.4}$	$10^{6.7}$	$10^{2.5}$	10^{3}	$10^{5.2}$
	Solar	**100.0**	0.04	1.66	0.4	0.1	5.05	99.6	2.2	1
TiO_2[s]	BSE	**100.0**	0.1	4.47	1.67	0.13	6.4	**99.9**	4.61	2.2
	Bulk crust	**100.0**	0.3	5.8	**29**	0.9	9.9	**99.9**	**45.2**	3.02
	Solar	0	2.79	**97.4**	0.7	1.07	3.9	0.002	0.8	13.4
Al_2O_3[s]	BSE	0	6	**94.2**	0.9	1.35	6.13	<0.001	1.2	17
	Bulk crust	0	**17.7**	**93.1**	3.6	6.3	16	<0.01	6.7	**45**
	Solar	0	0.15	0.47	0.01	0.01	0.35	<0.001	0.05	1.1
$CaTiO_3$[s]	BSE	0	0.16	1	0.03	0.05	0.35	0	0.07	1.0
	Bulk crust	0	0.7	0.7	0.13	0.16	0.96	0	0.4	2.6
	Solar	<0.001	<0.001	<0.001	5.15	6	<0.001	<0.001	<0.001	0
Fe_2O_3[s]	BSE	0	0	0	0.3	0.33	0	0	0	0
	Bulk crust	0	0	0	0.08	0.14	0	0	0	0
	Solar	0	0.08	<0.01	4.8	8.02	0.2	0.01	1.4	0.1
FeS[s]	BSE	0	0.05	4.2	1.7	2	0.1	<0.001	0.15	0.04
	Bulk crust	0	<0.01	0	1.36	1.86	0.02	0	0.04	<0.01
	Solar	0	<0.01	<0.01	5.6	5.6	0.2	0.01	0.5	0.05
FeO[s]	BSE	0	0	<0.001	1.11	1.25	0.02	<0.001	0.01	<0.01
	Bulk crust	0	0	0	0.85	1.16	<0.01	0	<0.01	<0.01
	Solar	0	**14.6**	0.34	3.3	3.3	**18.1**	0.01	4	**41.7**
Fe[s]	BSE	0	4.11	0.14	0.6	0.7	4	0	0.8	9.5
	Bulk crust	0	2.2	0.05	0.5	0.7	1.9	0	0.8	4.2
	Solar	0	9.7	0.08	**12.4**	**11.7**	**46.4**	0.05	**15**	**28**
SiO[s]	BSE	0	**45.9**	0.16	**13.4**	**13.4**	**66.4**	<0.001	**16.2**	**60.1**
	Bulk crust	0	**72.3**	0.16	**25**	**36.6**	**69.8**	<0.01	**35.6**	**44.5**
	Solar	0	**14.8**	<0.001	**14**	**13.2**	3.5	0.05	**15.7**	2.8
SiO_2	BSE	0	1.01	<0.001	**15.1**	**15**	2.32	<0.01	**10.0**	2.0
	Bulk crust	0	3.14	<0.01	**28.1**	**41.1**	0.8	<0.01	7.4	0.5
	Solar	0	5.1	<0.001	9.1	8.35	**10.5**	0.03	**11**	6.1
MgO[s]	BSE	0	**15.8**	<0.001	**12.3**	**12.5**	9	<0.01	**10.5**	5.0
	Bulk crust	0	0.6	<0.01	1.07	1.05	0.18	0	0.5	0.07
	Solar	0	**22.4**	<0.001	**23.1**	**23.1**	3.2	0.07	**24.2**	2
$MgSiO_3$[s]	BSE	0	6.05	0	**22.4**	**22.7**	1.9	<0.01	**22.1**	1.3
	Bulk crust	0	0.6	0	6.0	5.9	<0.01	<0.01	1.0	<0.01
	Solar	0	**30.2**	<0.001	**21.3**	**19.4**	8.3	0.07	**25.4**	3.6
Mg_2SiO_4[s]	BSE	0	**20.7**	0	**30.1**	**30.3**	3.3	<0.01	**34.1**	1.6
	Bulk crust	0	2.2	0	4.17	4.1	0.13	<0.01	2.06	0.05
Maximum nucleation rate	Solar		−8.1			12.13			5.98	
$\log_{10}J_{*,\,\rm max}$ (cm^{-3} s^{-1})	BSE		−9.75			11.86			4.42	
	Bulk crust		−8.91			12.35			4.74	
Cloud-averaged mean cloud particle radius	Solar		2.83			0.50			0.58	
$\langle a\rangle_{\rm avg}$ (μm)	BSE		3.58			0.47			0.43	
	Bulk crust		2.98			0.32			0.29	

increase the likeliness of cloud formation at or near the sub-stellar point. Such possibilities have not been ruled out by Demory et al. (2016b), wherein the large observed temperature gradient between the day and night sides may indeed favour cloud formation. They also find the hotspot to be shifted by 41°± 12°towards the east of the sub-solar point, which further augments the possibility of a strong circulation regime. Our cloud model indicates the possibility of a highly opaque cloud layer on 55 Cnc e with particles primarily consisting of Mg silicates (∼25 per cent), followed by Si oxides and a minor percentage of Fe, Al and Ca oxides.

Recent spectroscopic observations of 55 Cnc e by Tsiaras et al. (2015) suggest an atmosphere that has C/O ∼ 1 has a high concentration of HCN.

Our mineral cloud formation models show a large variation in particle sizes and compositions for different planetary scenarios and different sets of element abundances, as tabulated in Table 3.

The particle sizes are found to be the largest in the case of a giant gas planet, which is indicative of the denser atmosphere resulting in the availability of more condensing material. The particle sizes follow the order of gas giant > HD 149 026b > 55 Cnc e, with the largest particles found at the cloud base in each of the cases, below which the particles evaporate. The biggest particle sizes are 54 μm for the solar case, 3.6 μm for the BSE case and 3 μm for the BC giant gas planet case. These values change for 55 Cnc e to 0.5, 0.47 and 0.32 μm for the solar, BSE and BC cases, respectively. For HD 149 026b, we find maximum mean cloud particle radii of 0.6, 0.4, and 0.28-μm for the solar, BSE and BC cases, respectively.

The cloud particle number densities [n_d (cm^{-3})] are 10 times higher for the atmosphere of 55 Cnc e as compared to HD 149 026b, which will contribute to a higher cloud opacity on 55 Cnc e.

We observe a similarity in the cloud property trend due to the changes in element abundances in each of the planet cases where cloud formation happens. The particle sizes are found to be maximum with a solar and BSE composition for each of the planets. This is due to the higher Mg and O content in the atmosphere with these abundances, which results in faster material growth of species such as $MgSiO_3$[s] and Mg_2SiO_4[s]. The dust number density (n_d) is found to be the highest for a MORB atmosphere, which can be explained due to a higher Ti content, which results in more seed species (TiO_2) formation during the nucleation stage. The particle composition also follows a similar trend due to changes in element abundances. Mineral cloud particles in the BC, UC and MORB atmospheres are predominantly composed of SiO[s] and SiO_2[s] species, and their percentages vary proportionally with the changes in element abundances. Similarly, a BSE and solar atmosphere would have dust particles predominantly consisting of Mg_2SiO_4[s], $MgSiO_3$[s] and MgO[s]. The atmosphere of only a gas giant has pressures and temperatures suitable for the cloud base to form particles consisting of Al_2O_3[s] and Fe[s] species. Lee et al. (2015b) in their analysis for 3D cloud formation on HD 189 733b find similar high volume fractions of Fe and Al binding in their cloud particles and suggest a locally lower cloud opacity due to Al_2O_3[s] and high opacity due to Fe[s], which could alter the radiation propagation.

The results obtained in this work can be summarized as follows:

(1) Our models suggest the possibility of mineral cloud formation on 55 Cnc e and HD 149 026b. The atmosphere of CoRoT-7b or HRSE is found to be too warm on the day side for gas condensation to occur based on the atmosphere profile applied.

(2) Our results indicate that changes in element abundance compositions result in significant changes in the compositions of (mineral) cloud particles. Solar and BSE atmospheres primarily consist of Mg materials, whereas the BC, UC and MORB atmospheres consist of Si- and Fe-binding materials.

(3) The cloud particle properties for different compositions follow a trend of variation independent of local gas-phase pressures and temperatures. As an example, an atmosphere with a high abundance of a seed-forming species, such as Ti, which is found in the MORB composition, will have a larger cloud number density as compared to the BSE, BC and UC compositions due to a higher number of seed particles formed.

(4) The atmospheres of 55 Cnc e and HD 149 026b require strong element replenishment to be able to sustain cloud formation in the atmosphere. An atmosphere with no vertical replenishment results in the heavy elements raining out, rendering the atmosphere depleted of heavy elements.

Magma (or volcano) planets will form thick opaque clouds that will affect the evolution of these rocky planets, and with that maybe also the emergence of plate tectonics. With the bulk element abundances for extrasolar planets being very difficult to determine from present formation and evolutionary models, Table 3 provides global mean values for cloud properties for various rocky abundances as first guidance for retrieval methods and for planet evolution models.

ACKNOWLEDGEMENTS

We thank the referee for providing helpful feedback that led to further improvements of this paper. GM acknowledges an ERASMUS studentship from the TU Delft. ChH highlights financial support of the European Community under the FP7 by an ERC starting grant number 257431. YM greatly appreciates the CNES travel funding and post-doctoral fellowship programme. We are grateful to J. Fortney for providing us with the HD 149026b atmosphere structures. We would like to thank Paul Rimmer for useful discussions that helped to improve the manuscript.

REFERENCES

Agúndez M., Parmentier V., Venot O., Hersant F., Selsis F., 2014, A&A, 564, A73
Bilger C., Rimmer P., Helling C., 2013, MNRAS, 435, 1888
Cridland A. J., Pudritz R. E., Alessi M., 2016, MNRAS, 461, 3274
Demory B.-O. et al., 2011, A&A, 533, A114
Demory B.-O., Gillon M., Seager S., Benneke B., Deming D., Jackson B., 2012, ApJ, 751, L28
Demory B.-O., Gillon M., Madhusudhan N., Queloz D., 2016a, MNRAS, 455, 2018
Demory B.-O. et al., 2016b, Nature, 532, 207
Dressing C. D. et al., 2015, ApJ, 800, 135
Eistrup C., Walsh C., van Dishoeck E. F., 2016, A&A, 595, A83
Fegley B., Jacobson N. S., Williams K., Plane J., Schaefer L., Lodders K., 2016, ApJ, 824, 103
Fortney J., Saumon D., Marley M., Lodders K., Freedman R., 2006, ApJ, 642, 495
Fortney J. J., Lodders K., Marley M. S., Freedman R. S., 2008, ApJ, 678, 1419
Gao P., Benneke B., 2016, AAS/Division for Planetary Sciences Meeting Abstracts. p. 302.02
Gillon M. et al., 2012, A&A, 539, A28
Grevesse N., Asplund M., Sauval A., 2007, Space Sci. Rev., 130, 105
Guillot T., Burrows A., Hubbard W., Lunine J., Saumon D., 1996, ApJ, 459, L35
Helling C., Casewell S., 2014, A&AR, 22, 1
Helling C., Fomins A., 2013, Phil. Trans. R. Soc. A, 371, 20110581
Helling C., Woitke P., 2006, A&A, 455, 325
Helling C. et al., 2008a, MNRAS, 391, 1854
Helling C., Woitke P., Thi W.-F., 2008b, A&A, 485, 547
Helling C., Woitke P., Rimmer P. B., Kamp I., Thi W.-F., Meijerink R., 2014, Life, 4
Helling C. et al., 2016a, Surv. Geophys., 37, 705
Helling C. et al., 2016b, MNRAS, 460, 855
Ito Y., Ikoma M., Kawahara H., Nagahara H., Kawashima Y., Nakamoto T., 2015, ApJ, 801, 144
Jeong K. S., Winters J. M., Sedlmayr E., 1999, in Le Bertre T., Lebre A., Waelkens C., eds, Proc. IAU Symp. 191, Asymptotic Giant Branch Stars. Kluwer, Dordrecht, p. 233
Jeong K. S., Chang C., Sedlmayr E., Sülzle D., 2000, J. Phys. B At. Mol. Phys., 33, 3417
Khodachenko M. L., Shaikhislamov I. F., Lammer H., Prokopov P. A., 2015, ApJ, 813, 50
Kirkby J. et al., 2011, Nature, 476, 429
Knutson H. A., Benneke B., Deming D., Homeier D., 2014, Nature, 505, 66

Lee G., Helling C., Giles H., Bromley S. T., 2015a, A&A, 575, A11
Lee G., Helling C., Dobbs-Dixon I., Juncher D., 2015b, A&A, 580, A12
Lopez E. D., Rice K., 2016, MNRAS, preprint (arXiv:1610.09390)
McDonough W., Sun S.-s., 1995, Chem. Geol., 120, 223
Madhusudhan N., 2012, ApJ, 758, 36
Miguel Y., Kaltenegger L., 2013, ApJ, 780, 166
Miguel Y., Kaltenegger L., Fegley B., Schaefer L., 2011, ApJ, 742, L19
Mordasini C., van Boekel R., Mollière P., Henning T., Benneke B., 2016, ApJ, 832, 41
Moses J. I. et al., 2011, ApJ, 737, 15
Nelson B. E., Ford E. B., Wright J. T., Fischer D. A., von Braun K., Howard A. W., Payne M. J., Dindar S., 2014, MNRAS, 441, 442
Owen J. E., Mohanty S., 2016, MNRAS, 459, 4088
Palme H., Lodders K., Jones A., 2013, Treatise on Geochemistry, 2nd edn. Elsevier, p. 15. Available at: http://www.sciencedirect.com/science/article/pii/B9780080959757001182
Parmentier V., Showman A. P., Lian Y., 2013, A&A, 558, A91
Rimmer P. B., Helling C., Bilger C., 2014, Int. J. Astrobiol., 13, 173
Rogers L. A., 2015, ApJ, 801, 41
Sato B. et al., 2005, ApJ, 633, 465
Schaefer L., Fegley B., 2004, Icarus, 169, 216
Schaefer L., Fegley B., 2009, ApJ, 703, L113
Schaefer L., Lodders K., Fegley B., 2012, ApJ, 755, 41
Sudarsky D., Burrows A., Hubeny I., Li A., 2005, ApJ, 627, 520
Taylor S. R., McLennan S., 2009, Planetary Crusts: Their Composition, Origin and Evolution. Cambridge Univ. Press
Trammell G. B., Arras P., Li Z.-Y., 2011, ApJ, 728, 152
Tsiaras A. et al., 2015, ApJ, 820, 99
Winn J. N. et al., 2011, ApJ, 737, L18
Witte S., Helling C., Hauschildt P., 2009, A&A, 506, 1367
Witte S., Helling C., Barman T., Heidrich N., Hauschildt P., 2011, A&A, 529, A44
Woitke P., Helling C., 2003, A&A, 399, 297
Woitke P., Helling C., 2004, A&A, 414, 335

APPENDIX A: ELEMENT ABUNDANCES AND GROWTH SURFACE REACTIONS

A1 Terrestrial element abundances from rocks

The composition of a rock is expressed in terms of weight oxides in the geoscience literature. This is expressed in weight percentage of a particular compound; for example, the UC of the Earth is a mixture of 66.6 per cent SiO_2[s], 15.4 per cent Al_2O_3[s] and 3.59 per cent CaO[s]. In astronomical literature, element abundances are expressed relative to 10^{12} H atoms such that the element abundance ϵ_i for a certain species i is (i = Si, O, Mg, ...)

$$\log(\epsilon_i) = \log(\frac{n_i}{n_{\rm H}}) + 12. \quad \text{(A1)}$$

Here, n_i (cm^{-3}) is the number density of the element i; hence, $n_{\rm H} = 10^{12}$. The weight oxide (per cent) of each material (SiO_2[s], FeO[s], Al_2O_3[s], etc.) is used to calculate the number of moles of that compound in a particular rock type as

$$M(\text{number of moles}) = \frac{m(\text{ per cent of compound})}{n[\text{molar mass (g mole}^{-1})]}. \quad \text{(A2)}$$

The number of moles of a particular element, for example, oxygen(O) in SiO_2[s] is calculated as

$$M_{\rm O} = \nu_{\rm O} M. \quad \text{(A3)}$$

ν_i is the stoichiometric coefficient of the chosen element in the compound. The total number of atoms of a particular element can then be derived from

$$N_{{\rm tot},i} = N_{\rm A} \sum \nu_s M_{i,s}. \quad \text{(A4)}$$

$n_{{\rm tot},i}$ is the total number of moles of a particular element in the mixtures, s is the compound (SiO_2[s], Al_2O_3[s], FeO[s], etc.) and $N_{\rm A}$ (atoms mole^{-1}) is Avogadro's number.

The rock composition in Tables A1 and 1 does not contain information about the potential hydrogen content that a rocky planet's atmosphere may have. Thus, we follow the method generally used to calculate the element abundances from meteorites where the abundance ratios are calculated with respect to the Si atoms in a scale of $\log_{10}\epsilon_{\rm Si} = 6$,

$$\log(\epsilon_{\rm Si}) = \log(\frac{n_{{\rm tot},i}}{n_{\rm Si}}) + 6. \quad \text{(A5)}$$

To be able to convert the Si-normalized abundances into an H-normalized abundance scale, we follow the method outlined by Palme, Lodders & Jones (2013). The conversion factor between the two scales was calculated by dividing the H-normalized solar abundances by the Si-normalized meteorite abundances. The comparison was made for all elements with an error of the corresponding photospheric abundance of less than 0.1 dex, i.e. less

Table A1. Weight (per cent) of oxides for various types of Earth and magma rocks.

Weight oxide (per cent)	Komatite[a]	BSE[b]	BSE[c]	MORB[c]	UC[d]	BC[d]
SiO_2	47.10	45.97	45.1	49.6	66.6	60.6
MgO	29.60	36.66	37.9	9.75	2.5	4.
FeO	–	8.24	8.06	8.06	5.04	6.71
Al_2O_3	4.04	4.77	4.46	16.8	15.4	15.9
CaO	5.44	3.78	3.55	12.5	3.59	6.40
Na_2O	0.46	0.35	0.36	2.18	3.27	3.07
Cr_2O_3	–	–	0.38	0.07	0.0003	0.0004
TiO_2	0.24	0.18	0.2	0.9	0.64	0.72
K_2O	0.09	0.04	0.03	0.07	2.8	1.81
P_2O_5	–	–	0.02	0.1	0.13	0.15
Fe_2O_3	12.8	–	–	–	–	—

Notes. [a]Schaefer & Fegley (2004), [b]O'Neill & Palme (1998), [c]McDonough & Sun (1995), [d]Taylor & McLennan (2009), and [e]Grevesse et al. (2007).

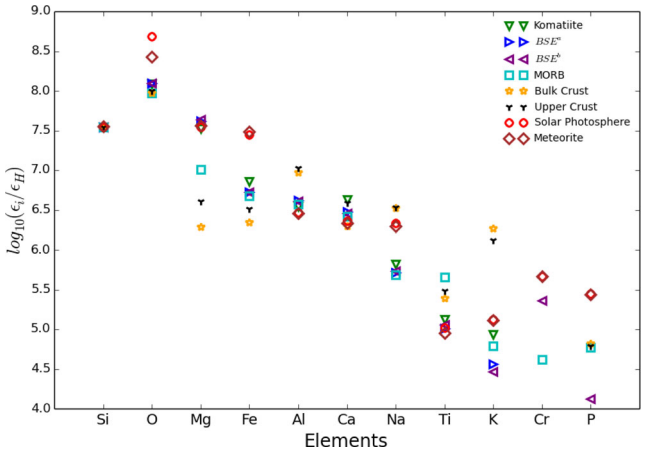

Figure A1. Element abundance [$\log_{10}(\epsilon_{\rm H}) = 12$ scale] for six Earth rock and magma compositions. The komatite and BSE^a compositions are used by Miguel et al. (2011), and BSE^b, MORB, BC and UC compositions are used by Ito et al. (2015) (see Tables A1 and 1). The solar photospheric and meteorites abundances are shown for comparison (Grevesse et al. 2007).

than 25 per cent. The log of the average ratio of solar abundance per 10^{12} H atoms/meteorite abundance per 10^6 silicon atoms is 1.546 ± 0.045 (Palme et al. 2013). Thus,

$$\log(\epsilon_{\rm H}) = \log(\epsilon_{\rm Si}) + 1.546. \quad \text{(A6)}$$

The resulting element abundances in the $\log(\epsilon_{\rm H}) = 12$ scale are listed in Table 1. In Fig. A1, we compare the element abundances derived for all the six types of rocks [BC – yellow stars, UC – black, MORB – light-blue squares (metal-oxide-ridge basalt), BSE^a – blue triangle (bulk silicate Earth), BSE^b – purple triangle and komatite – green triangle]. We include a comparison to the solar (red circles) and the meteorite (brown diamonds) element abundances.

A2 Surface-growth reactions

Table A2. Extended set of surface growth reactions for the growth of dust particles in addition to table 1 in Helling et al. (2008b). The total sum of surface growth reactions taken into account here is 79.

Index r	Solid[s]	Surface reaction	Key species
61.	MgO[s]	$2MgH + 2H_2O \longrightarrow 2MgO[s] + 3H_2$	MgH
62.	$MgSiO_3$[s]	$2MgH + 2SiO + 4H_2O \longrightarrow 2MgSiO_3[s] + 5H_2$	min{MgH, SiO}
63.		$MgH + SiH + 3H_2O \longrightarrow MgSiO_3[s] + 4H_2$	min{MgH, SiH}
64.		$2MgH + 2SiN + 6H_2O \longrightarrow 2MgSiO_3[s] + 7H_2 + N_2$	min{MgH, SiN}
65.		$MgS + Si + 3H_2O \longrightarrow MgSiO_3[s] + H_2S + 2H_2$	min{MgS, Si}
66.		$2MgN + 2Si + 3H_2O \longrightarrow 2MgSiO_3[s] + 3H_2 + N_2$	min{MgN, Si}
67.	Mg_2SiO_4[s]	$2MgH + SiO + 3H_2O \longrightarrow Mg_2SiO_4[s] + 4H_2$	min{2MgH, SiO}
68.		$4MgH + 2SiH + 8H_2O \longrightarrow 2Mg_2SiO_4[s] + 11H_2$	min{2MgH, SiH}
69.		$4MgH + 2SiN + 8H_2O \longrightarrow 2Mg_2SiO_4[s] + N_2 + 10H_2$	min{2MgH, SiN}
70.		$2MgS + Si + 4H_2O \longrightarrow Mg_2SiO_4[s] + 2H_2S + 2H_2$	min{2MgS, Si}
71.		$2MgN + Si + 4H_2O \longrightarrow 2Mg_2SiO_4[s] + N_2 + 4H_2$	min{2MgN, Si}
72.	SiO_2[s]	$2SiH + 4H_2O \longrightarrow 2SiO_2[s] + 5H_2$	SiO
73.		$2SiN + 4H_2O \longrightarrow 2SiO_2[s] + N2 + 4H_2$	SiN
74.	SiO[s]	$2SiH + 2H_2O \longrightarrow 2SiO[s] + 3H_2$	SiO
75.		$2SiN + 2H_2O \longrightarrow 2SiO[s] + N_2 + 2H_2$	SiN
76.	Fe[s]	$2FeH + H_2 \longrightarrow 2Fe[s] + 2H_2$	FeH
77.	FeO[s]	$2FeH + 2H_2O \longrightarrow 2FeO[s] + 3H_2$	FeH
78.	FeS[s]	$2FeH + 2H_2O \longrightarrow 2FeS[s] + 3H_2$	FeH
79.	Fe_2O_3[s]	$2FeH + 3H_2O \longrightarrow Fe_2O_3[s] + 4H_2$	FeH

This paper has been typeset from a TEX/LATEX file prepared by the author.